OXIDATION BEHAVIOR OF $(Co,Mn)_3O_4$ COATINGS ON PREOXIDIZED STAINLESS STEEL

by

Kathryn Olivia Hoyt

A thesis submitted in partial fulfillment
of the requirements for the degree

of

Master of Science

in

Chemical Engineering

MONTANA STATE UNIVERSITY
Bozeman, Montana

April 2011

©COPYRIGHT

by

Kathryn Olivia Hoyt

2011

All Rights Reserved

APPROVAL

of a thesis submitted by

Kathryn Olivia Hoyt

This thesis has been read by each member of the thesis committee and has been found to be satisfactory regarding content, English usage, format, citation, bibliographic style, and consistency and is ready for submission to the The Graduate School.

Dr. Paul Gannon

Approved for the Department of Chemical and Biological Engineering

Dr. Ron Larsen

Approved for The Graduate School

Dr. Carl A. Fox

STATEMENT OF PERMISSION TO USE

In presenting this thesis in partial fulfillment of the requirements for a master's degree at Montana State University, I agree that the Library shall make it available to borrowers under rules of the Library.

If I have indicated my intention to copyright this thesis by including a copyright notice page, copying is allowable only for scholarly purposes, consistent with "fair use" as prescribed in the U.S. Copyright Law. Requests for permission for extended quotation from or reproduction of this thesis in whole or in parts may be granted only by the copyright holder.

Kathryn Olivia Hoyt

April 2011

ACKNOWLEDGEMENTS

I would like to thank the Image and Chemical Analysis Laboratory at Montana State University for use of the Scanning Electron Microscope**,** the Time of Flight-Secondary Ion Mass Spectrometer and the X-Ray Diffraction as well as important help from ICAL staff. I would also like to thank the Montana Microfabrication Facility, for use of the Magnetron Sputtering deposition equipment. I greatly appreciate Rukiye Tortop, Brian Ellingwood, Hamed Khoshuei, Chandra Macauley, and Dr. Roberta Amendola for their help with experiments. This work was funded in part by NSF-EPSCOR. I am thankful for the support and guidance from my advisor Dr. Paul Gannon, as well as Sheree Watson, Preston White and my family and friends. I am grateful also to the American Indian Science and Engineering Society and the Indigenous Women in Science Network for continued inspiration.

TABLE OF CONTENTS

1. INTRODUCTION 1

SOFC Interconnects and coatings 1
Defect Chemistry 5
Oxidation Kinetics 6
Oxidation Thermodynamics 7
Electronic Conduction 8

2. EXPERIMENTAL PROCEDURES 10

Sample Preparation 10
Preoxidation 10
CoMn Coating Deposition 11
CoMnO Coating Deposition 12
Exposures 12
Oxidation in Laboratory Air 12
Dual Atmosphere 12
ASR 13
Adhesion Assessment 13
Analysis Techniques 13
Cross Sectioning and Polishing 13
Time of Flight Secondary Ion Mass Spectrometry 14
X-Ray Diffraction 14
Thermogravimetric Analysis 14

3. RESULTS 16

Elemental Transport and Thickness 16
Surface Morphology 24
Coating Deposition Investigation 27
Phase Development 30
Thermogravimetric Analysis 33
Dual Atmosphere 34
ASR 36
Adhesion Assessment 37

4. DISCUSSION 39

Elemental Transport and Thickness 39
Surface Morphology 42
Coating Deposition Investigation 42

TABLE OF CONTENTS - CONTINUED

Phase Development....43
Thermogravimetric Analysis....43
Dual Atmosphere....44
ASR....46
Adhesion Assessment....48

5. CONCLUSIONS....49

REFERENCES CITED....51

LIST OF TABLES

Table Page

1.1 Kroger-Vink Notation. ……..……..……5

2.1 Composition of 441HP ferritic stainless steel……..……..10

2.2 Experimental and sample identification matrix.……..……..11

LIST OF FIGURES

Figure Page

1.1 Solid Oxide Fuel Cell and related reactions 1

1.2 Solid Oxide Fuel Cell Stack 2

3.1 Cross section EDS elemental line scans of: a.) 0pre-0ox
b.) 3pre-0ox c.) 10pre-0ox d.) 100pre-0ox 17

3.2 Cross section EDS elemental line scans of: a.) 0pre-10ox
b.) 3pre-10ox c.) 10pre-10ox d.) 100pre-10ox 18

3.3 Cross section EDS elemental maps of: a.) 0pre-10ox
b.) 3pre-10ox c.) 10pre-10ox d.) 100pre-10ox 19

3.4 Cross section EDS elemental line scans of: a.) 0pre-100ox
b.) 3pre-100ox c.) 10pre-100ox d.) 100pre-100ox 20

3.5 Cross section EDS elemental maps of: a.) 0pre-100ox
b.) 3pre-100ox c.) 10pre-100ox d.) 100pre-100ox 21

3.6 Cross section EDS elemental line scans of:
a.) 0pre-1650ox b.) 100pre-1650ox 22

3.7 Cross section EDS elemental maps of:
a.) 0pre-1650ox b.) 100pre-1650ox 23

3.8 Micrographs of coating surface of: a.) 0pre-0ox
b.) 3pre-0ox c.) 10pre-0ox d.) 10opre-0ox 24

3.9 Micrographs of coating surface of: a.)0pre-10ox
b.) 3pre-10ox c.) 10pre-10ox d.) 100pre-10ox 25

3.10 Micrographs of coating surface of: a.)0pre-100ox
b.) 3pre-100ox c.) 10pre-100ox d.) 100pre-100ox 26

3.11 Scanning electron micrographs of 0pre-1650ox 26

3.12 Scanning electron micrographs of 100pre-1650ox 27

3.13 Cross sections EDS line scans of: a.) 0pre-10ox-Ox
b.) 0pre-10ox-Met c.) 10pre-10ox 28

LIST OF FIGURES-CONTINUED

Figure Page

3.14 TOF-SIMS sputtered depth profiles for 0pre-10ox-Ox 29

3.15 TOF-SIMS sputtered depth profiles for 0pre-10ox-Met..... 29

3.16 TOF-SIMS sputtered depth profiles for 10pre-10ox 30

3.17 XRD patterns of: Bare stainless steel, 0pre-0ox,
10pre-0ox, 100pre-0ox..... 31

3.18 XRD patterns of: Bare stainless steel oxidized for 10 hours,
0pre-10ox, 10pre-10ox, 100pre-10ox 32

3.19 XRD patterns of: Bare stainless steel oxidized for 100 hours,
0pre-100ox, 10pre-100ox, 100pre-100ox 33

3.20 Thermogravimetric Analysis of samples preoxidized
for 0 or 3 hours..... 34

3.21 Cross section EDS elemental line scans of:
a.) 0pre-Dual b.) 3pre-Dual..... 35

3.22 Cross section EDS elemental line scans of:
a.) 0pre-Air b.) 3pre-Air..... 36

3.23 Area Specific Resistance test with
platinum connection paste at 800°C 37

3.24 Optical microscope images of
Rockwell Indenter Adhesion Test..... 38

4.1 Conceptual graphic of oxidation behavior of
a.) Preoxidized samples, coatings deposited as metal
b.) non-preoxidized samples, coatings deposited as metal
c.) non-preoxidized samples, coatings deposited as oxide 39

ABSTRACT

As global energy challenges grow, alternative energy technologies like fuel cells are being investigated. Solid Oxide Fuel Cells (SOFCs) provide the advantages of high energy conversion efficiency, low emissions, fuel flexibility and both portable and stationary application. High material cost and need for longer material lifespan still impede the wider use of SOFCs. To produce substantial voltage, planar SOFCs are joined into stacks using interconnects. Interconnects both separate and connect each individual fuel, separating gas flow and conducting current. For SOFCs that operate at less than 800°C, metal alloys are being considered for the interconnect, particularly ferritic stainless steel. Ceramic coatings are being explored to improve the surface conductivity over time and significantly reduce Cr volatility from the steel. In addition, the coating must have a matching coefficient of thermal expansion (CTE) and be compatible with electrode and seal materials. One promising coating is $(Co,Mn)_3O_4$ spinel, which is deposited using various techniques, resulting in different thicknesses, compositions and microstructures.

In this study, stainless steel 441HP samples were subjected to three levels of preoxidation prior to coating with 2 μm CoMn alloy using magnetron sputtering. Samples were subsequently annealed to $Co_{1.5}Mn_{1.5}O_4$ in 800°C air. Oxidation behaviors were evaluated as a function of exposure to laboratory air and dual atmospheres (3% H_2O and H_2 on one side, 3% H_2O and air on the other) and area specific resistance (ASR) measurements in lab air, all at 800°C. In addition, chemical and phase composition, mass gain, and adhesion were investigated using a complimentary suite of analytical techniques. Preoxidation was found to inhibit Fe transport from the stainless steel into the coating and exhibited a substantially thinner surface oxide layer after oxidation. Preoxidized samples also maintained slightly lower ASR values after 1650 hours in 800°C air compared to non-preoxidized samples. Oxidation behaviors, their possible mechanisms, and implications for SOFC interconnects will be presented and discussed.

CHAPTER 1

INTRODUCTION

Solid Oxide Fuel Cell Interconnects

To address growing global energy concerns, solid oxide fuel cell (SOFC) technology is being developed. SOFCs electrochemically oxidize hydrogen or hydrocarbon fuels, generating electricity and heat. SOFCs offer advantages over other fuel cells. These advantages include very high energy conversion efficiency and fuel flexibility. SOFCs are also appealing relative to combustion due to their higher efficiency and cleaner emissions, while still maintaining their potential for both stationary and portable applications. In Figure 1.1 an SOFC with relevant reactions is presented [1].

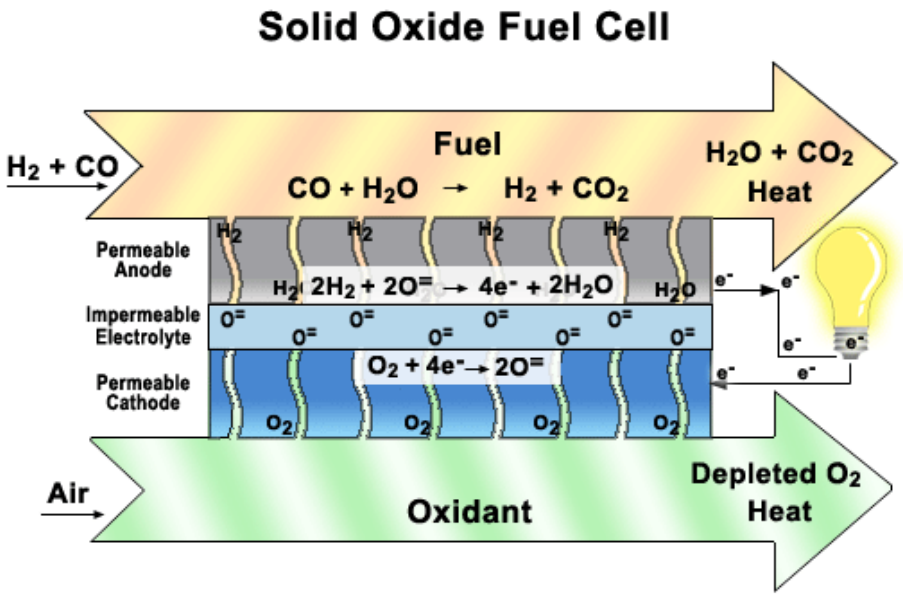


Figure 1.1 Solid Oxide Fuel Cell and related reactions

To produce a substantial voltage, individual fuel cells are joined by interconnects to form a fuel cell stack. Interconnects provide mechanical strength and compartmentalized flow of the fuel and air to their respective electrodes. The interconnect must also conduct electrical current through the stack at high operating temperatures (600-1000°C) over the device lifetime of 40,000 hours. A fuel cell stack is shown in Figure 1.2 [2].

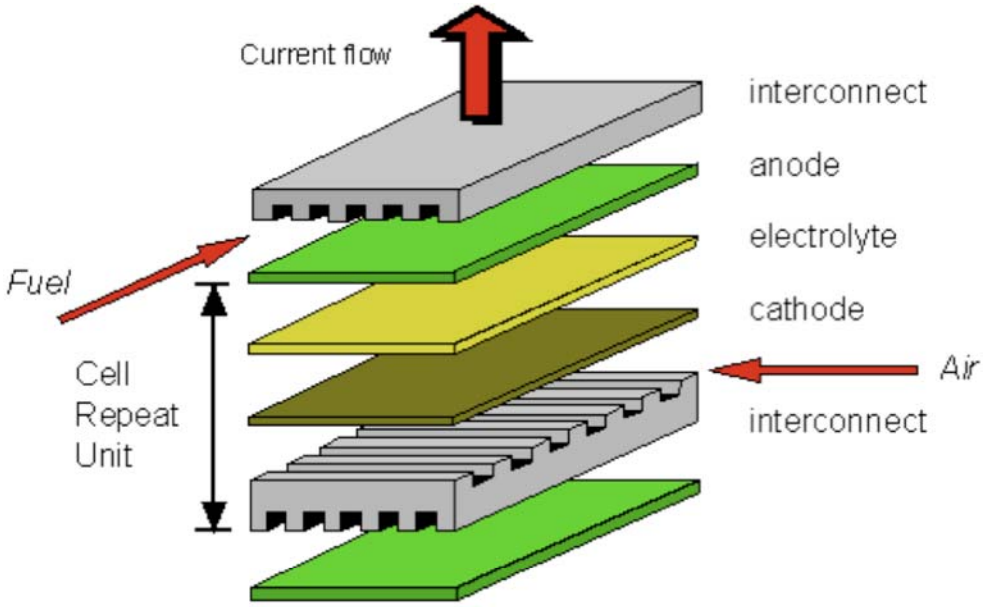


Figure 1.2 Solid Oxide Fuel Cell Stack

Detailed discussions of SOFC stacks, components and operation can be found elsewhere [3, 4]. SOFC stacks are required to establish a sufficient electric potential. The components in addition to the interconnect include the anode to which fuel is supplied, the cathode to which air is supplied, electrolyte, and hermetic seals. Promising cathode materials include strontium-doped lanthanum manganites (LSM), lanthanum strontium cobalt ferrite (LSCF) and lanthum nickel ferrite (LNF). Electrolytes are most commonly yitria stabilized zirconia (YSZ), though scandium doped zirconia (ScSZ), ceria-based

electrolytes or magnesium and strontium doped lanthanum gallate are also being considered [5]. Electrolytes in SOFCs are usually oxygen anion conducting [5]. Anodes are often Ni-YSZ cermet, Ni for electronic conductivity and YSZ for oxygen ion conductivity. The triple phase boundary, where the gas, electrode and electrolyte touch, is where most of the electrochemistry happens within the cell.

When cell operating temperature was still greater than 1000°C lanthanum chromite was the best interconnect candidate due to its stability in reducing and oxidizing atmospheres at high temperatures and its electrical conductivity [6]. Lanthanum chromite-based coatings have also been investigated for use with alloys [7].

Due to cell and stack design innovations, some SOFCs now operate at 600-800°C, which permits the use of stainless steel for the interconnect, an inexpensive and commercially available material that has good manufacturability [8-11]. Ferritic stainless steel has a body-centered cubic structure with a Cr composition of approximately 17-22%. Ferritic stainless steel forms a chromia-based thermally grown oxide (TGO) surface layer at high temperatures, which remains more conductive over time than alumina forming alloys. Also, the coefficient of thermal expansion (CTE) for ferritic stainless steel matches adjoining SOFC components [8-10]. During SOFC operation, manganese containing ferritic stainless steels, like 441HP, form a duplex surface oxide layer, comprised of a chromia-rich sublayer and a $(Fe,Mn,Cr)_3O_4$ spinel top layer [12]. Surface oxide layers provide a barrier to hydrogen permeation through the steel ensuring the gas flows remain compartmentalized [13]. This surface oxide layer has been investigated as a protective coating but has not been found to be sufficient for SOFC

application. Ultimately, the chromia-based layer on the stainless steel at high temperatures can cause chromium poisoning of the fuel cell and decreased conductivity over time as the surface layer thickens [8-10].

Under SOFC conditions, steel interconnects are subjected to electric current and dual atmospheres (moist hydrogen gas on one side, moist air on the other). Oxidation behavior is complex and dynamic under these conditions. Dual atmosphere and moisture exacerbate Fe transport into the oxide scale, increase oxidation rate and different phases can evolve as compared to dry single atmospheres [14].

An oxide coating decreases the partial pressure of oxygen at the surface of the stainless steel, limiting the growth of the chromia layer [10]. Spinels, of the form AB_2O_3, depending on the ions in the A and B sites, have been considered due to their close CTE match with ferritic stainless steel, electronic conductivity and ability to absorb Cr ions [8]. Face-centered cubic (FCC) in structure, the A and B are divalent, trivalent and quadrivalent cations in the octahedral and tetrahedral sites while the oxygen anions fill the FCC lattice sites [8].

$Co_{1.5}Mn_{1.5}O_4$ spinel meets many of the requirements for an interconnect coating. $Co_{1.5}Mn_{1.5}O_4$ has a comparable CTE to stainless steel, anode and cathode materials [8]. The CTE of $Co_{1.5}Mn_{1.5}O_4$ is 11.4 x 10^{-6}/K [15]. The CTE of Ferritic Stainless Steel is 11-13 x 10^{-6}/K [16, 17]. In addition, outward Cr transport from the stainless steel toward the oxidative interface is significantly inhibited by the presence of the $Co_{1.5}Mn_{1.5}O_4$ coating [18-23]. This conductive ceramic oxide coating has demonstrated the ability to maintain a low area specific resistance (ASR) in the high operating temperatures of a SOFC [15, 16-

23]. An improvement in ASR and decreased outward Cr transport is also accomplished by deposition of $MnCo_{1.9}Fe_{0.1}O_4$ coatings relative to bare steel [24].

The effects of a thermally grown oxide (TGO) surface layer on the stainless steel prior to coating deposition is a treatment beginning to be investigated [19, 25]. The effect of different amounts of preoxidation and the mechanism of the oxidation behavior of preoxidized and coated stainless steel are not well understood. This study intends to expand understanding of preoxidized and coated stainless steel, particularly of attributes related to coated SOFC interconnects, such as oxidation behaviors in single (air) and dual (H_2/air) atmospheres, adhesion, as well as long term (1650 hour) ASR.

Defect Chemistry

It is customary to use Kroger-Vink notation when discussing the defect chemistry of ionic solids, like solid oxides. Ionic transport occurs in solids through interstitial sites and vacancies in the crystal lattice.

Table 1.1 Kroger-Vink Notation

M_M	Metal atom on a metal site, no charge
V_M''	Vacancy on a metal site, -2 charge
O_O	Oxygen atom on an oxygen site, no charge
$V_O^{\cdot\cdot}$	Vacancy on an oxygen site, +2 charge
$M_i^{\cdot\cdot}$	Metal ion in an interstitial site, +2 charge
O_i''	Oxygen atom on an interstitial site, -2 charge
e’	electron in conduction band
h•	electron hole in valence band

In ionic solids, Frenkel and Schottky defects are common. Schottky defects occur under circumstances with equal amounts of cation and anion vacancies combined with

electronic defects. Frenkel defects occur with cation vacancies, interstitial cations and electronic defects, and are common in protective oxide scales.

The partial pressure of oxygen and the alloy composition determine the direction in which the oxide layer grows. Oxide scales in which cations transport outwardly grow at the oxide gas interface. Oxide scales that grow by inward diffusion of oxygen anions through anion vacancies in the oxide grow at the alloy-oxide interface.

Oxidation Kinetics

After an oxide layer nucleates and forms a continuous layer, oxidation of metal occurs by the transport of cations from the metal to the gas interface or by the transport of oxygen ions to the metal oxide interface. Oxidation kinetics are often diffusion-limited as the oxide scale becomes thicker.

$$M + O => MO$$

Oxygen molecules adsorb then dissociate into anions and either transport through the oxide to the metal alloy interface or cations transport outwardly and meet anions at the gas interface to form oxide. Chromia probably forms by outward cation transport which occurs by the flux of metal cations outward to meet oxygen ions at the gas interface while cation vacancies transport inward.

Diffusion limited oxidation rates are expected to follow the parabolic rate law:

$$(\Delta m)^2 = kt + C_1$$

where the change in mass, Δm, squared is equal to the rate constant multiplied by time plus a constant describing the initial oxide scale present before high temperature exposure

[26]. The constant k is known to decrease with the presence of a coating [27]. The parabolic reaction rate law for diffusion limited oxidation was first shown by Wagner [28].

Chromia, is generally considered to be a metal deficient p-type conductor when in oxidizing conditions. This means that chromium cations and electrons transport outward to the gas interface where the chromia forms vacancies and holes transport inward. In addition, spinel (AB_2O_4) can form from the oxidation of steel, commonly of the form $(Cr,Mn,Fe)_3O_4$. [12] This depends on the steel composition and exposure conditions as well. Moisture increases the oxidation rate by introducing the presence of protons that form hydroxide defects in the solid oxide [14, 29]. To maintain electroneutrality, metal vacancies form and this increases the solubility of cations into the oxide and consequently accelerates oxidation.

Oxidation Thermodynamics

Thermodynamic equilibrium determines which phases are favored during oxidation. The oxidation behavior of stainless steels depends upon the composition of the alloy as well as the composition of the atmosphere, temperature and pressure. From the Second Law of Thermodynamics, a negative Gibbs Free Energy implies a spontaneous formation. A generic reaction:

$$aA + bB = cC + dD$$

then it follows that:

$$\Delta G' = \Delta G^\circ + RT \ln\left(\frac{a_c^c a_D^d}{a_A^a a_B^b}\right)$$

where ΔG' is the Gibbs Free Energy of Formation for the given conditions, ΔG° is the Gibbs Free Energy of Formation for standard conditions, R is the gas constant, T is the temperature and a is the thermodynamic activity. The activity is determined by how the partial pressure of the species deviates from standard state and for ideal gasses and can be defined as:

$$a_i = \frac{p_i}{p_i^\circ}$$

where p_i is the partial pressure of species i and p_i° is the partial pressure of species i at standard state [28]. If we consider the oxidation reaction, then the solid states of the alloy and the oxide become 1 and we are left with

$$\Delta G' = \Delta G^\circ + RT \ln\left(\frac{p_{O_2}^\circ}{p_{O_2}}\right)$$

which shows that formation of an oxide phase depends on the partial pressure of oxygen, the temperature, and the standard state Gibbs Free Energy of the phase. Selective oxidation occurs due to differing Gibbs Free Energy of Formation of different oxides [28].

Electronic Conduction

To maintain electroneutrality, electronic defects, such as electron holes, form to compensate ionic defects. Electron holes form from the absence of an electron which occurs by an electron moving from the valence band to the conduction band [28, 30]. Electrons and electron holes move through semiconductors by hopping between host ions. The material can be a p-type conductor, referring to charge carried by positive

carriers (holes) or an n-type conductor, referring to charge carried by negative carriers (electrons). Electronic conductivity is usually an order of magnitude higher than ionic conductivity and therefore we focus mainly on ionic transport.

The remainder of the thesis will be organized into five chapters as: Chapter 2: Experimental Procedures, where sample preparation, exposures and analysis will be explained; Chapter 3: Results, where data from analysis is presented without interpretation; Chapter 4: Discussion, where data are interpreted and put into context of application; and Chapter 5: Conclusions, where findings are summarized to emphasize salient outcomes of research and their implications for SOFCs.

CHAPTER 2

EXPERIMENTAL PROCEDURES

Sample Preparation

Commercial ferritic stainless steel 441HP sheet, provided by ATI Alleghany Ludlum Inc. (1mm thick), was laser cut into 1 x 2 cm coupons; its nominal composition of major alloying elements is presented in Table 2.1.

Table 2.1 Composition of 441HP ferritic stainless steel.

Wt % steel	Fe	Cr	Nb	Mn	Si	Ni	Ti	Al
441HP	Bal	18.0	0.50	0.35	0.34	0.30	0.22	0.05
Tolerance	Bal	17.5-19.5	0.3+(9xC)min 0.9 max	1.00 max	1.00 max	1.00 max	0.10-0.50	-

Preoxidation

Samples were preoxidized in 800°C laboratory air for 0, 3, 10, or 100 hours before coating deposition. Time does not include exposure during the ramping (5°C/minute). An experimental matrix describing samples with respect to preparation and exposure is presented in Table 2.2; each sample was subjected to only one exposure and is identified within the respective cell. Surface analysis was conducted after exposures to investigate oxidation behavior in laboratory air, moist air only, and moist dual atmosphere, as well as during ASR measurements. For example, the sample that was preoxidized for 10 hours, coated with a CoMn metal coating, and then oxidized in laboratory air for 100 hours is labeled 10pre-100ox. The samples with the prefix 0pre-

10ox are distinguished by their coating deposition as either a metal (Met suffix) or an oxide (Ox suffix).

Table 2.2 Experimental and sample identification matrix.

Exposure ↓	Preoxidation Time (Hours)			
	0	3	10	100
Oxidation, 0 hrs	0pre-0ox	3pre-0ox	10pre-0ox	100pre-0ox
Oxidation, 10 hrs	0pre-10ox-Met 0pre-10ox-Ox	3pre-10ox	10pre-10ox	100pre-10ox
Oxidation, 100 hrs	0pre-100ox	3pre-100ox	10pre-100ox	100pre-100ox
Oxidation, 1650 hrs	0pre-1650ox			100pre-1650ox
Dual atmosphere, 300hrs	0pre-Dual	3pre-Dual		
Air-air, 300hrs	0pre-Air	3pre-Air		
ASR, 1650 hrs	0pre-ASR			100pre-ASR

CoMn Coating Deposition

Prior to coating deposition, samples were cleaned in a sonic wash, first for 10 minutes in acetone and then for 10 minutes in methanol. Samples were sputter cleaned in an Argon plasma for 90 seconds and then coatings were deposited using a magnetron sputtering system with a CoMn alloy target with a 1:1 atomic ratio. An amorphous CoMn metallic coating was deposited on room temperature substrates over four and a half hours using 300 W, DC power and 5 mTorr of Argon. Substrates were positioned 120 mm above the targets and rotated to promote uniformity. These deposition

parameters resulted in a coating thickness of ~2 μm, and were identical for every sample except the oxide deposited sample.

CoMnO Coating Deposition

Some samples were coated with CoMn sputtered in an oxygen atmosphere resulting in a $(Co,Mn)_3O_4$ coating deposited as an oxide. These samples were then oxidized for 10 hours and 100 hours in 800°C laboratory air and were not preoxidized prior to coating deposition.

Exposures

Oxidation in Laboratory Air

Coated samples of each preoxidation level were oxidized for exposure times of 0, 10, or 100 hours in 800°C laboratory air, with no control of flow or humidity. Witness samples from electrical resistance testing (ASR) were also evaluated for oxidation times of 1650 hours. The surface morphology of the coatings were analyzed using Field Emission Scanning Electron Microscopy (FEM).

Dual Atmosphere

Dual atmosphere behavior was investigated by subjecting circular sample coupons of diameter 2.5 cm to moisturized hydrogen (3% H_2O) on one side and moisturized air (3% H_2O) on the other for 300 hours, following preoxidation and coating. A custom dual atmosphere apparatus supplied a hydrogen flow rate of 30 mL/min and an air flow rate of 60 mL/min at 800°C as described elsewhere [31].

ASR

ASR was measured using pairs of identical samples, one non-preoxidized pair (0pre-ASR sample pair from Table 3), and one 100 hour preoxidized pair (100pre-ASR sample pair from Table 3). To ensure that a $(Co,Mn)_3O_4$ coating was present, both pairs of samples were oxidized for 100 hours in 800°C air before ASR measurement. Porous platinum paste was used for electrodes as described elsewhere [32]. Temperature was increased to 800°C in laboratory air and measurements were then initiated. A constant DC power current density of 0.5 A/cm^2 was applied and voltage was measured for 1650 hours in 800°C air. Coated witness samples from the ASR tests were cross-sectioned and polished for elemental analysis.

Adhesion Assessment

Coating adhesion was qualitatively assessed using Rockwell C Indentation with a 150 kg load combined with microscopy of the indented area to evaluate delamination behavior. This method, commonly referred to as the Daimer-Benz test, was developed by the Union of German Engineers and has been used by other SOFC investigators [33].

Analysis Techniques

Cross Sectioning and Polishing

Samples were prepared for microscopy by cross-sectioning and precision polishing. After using a diamond saw to slice perpendicularly through the sample layers, glass was secured to the coating side using epoxy. The sample was then polished using a series of diamond-embedded films. To reduce charging from the electron beam in the

Scanning Electron Microscope (SEM), a 15nm layer of Iridium was sputtered onto the polished cross section to create a conductive surface. The samples were investigated using SEM, FEM, and Energy Dispersive X-Ray Spectroscopy (EDS).

Time of Flight-Secondary Ion Mass Spectrometry

The coating composition was also analyzed using Time-of-Flight Secondary Ion Mass Spectrometry (TOF-SIMS). The sputtering size was 30 μm and analysis raster size was 12 μm. All samples were analyzed this way with sputtering times averaging 8 minutes.

X-Ray Diffraction

X-Ray Diffraction (XRD) was carried out using a thin-film detector on a standard XRD. 1kV of Cu-k-alpha x-rays were provided and the tube and detector rotated through 15-90 degrees in 2-theta geometry.

Thermogravimetric Analysis

Thermogravimetric analysis (TGA) was used to measure the mass change of the samples over time that occurs at 800°C in laboratory air. Ten sample coupons were preoxidized for 3 hours (plus ramping) at 800°C in laboratory air in quartz crucibles and ten other coupons were not preoxidized. All 20 coupons were coated on both sides with amorphous metal CoMn. Each coupon was placed in a quartz crucible, weighed and placed in the same oven. The oven ramped to 800°C at 5°C/min then remained at 800°C for the duration of data collection. For each time increment, one non-preoxidized and one preoxidixed coupon was removed with long tweezers and placed in a room temperature

oven with the door open to cool. The pair was then weighed 24 hours later when cool. A coupon for each time increment was used to improve statistical validity and to reduce the effects of multiple temperature cycles.

CHAPTER 3

RESULTS

Elemental Transport and Thickness

Preoxidation treatments established a chromia-based surface layer on the stainless steel prior to CoMn deposition. In non-preoxidized samples, the CoMn coating was deposited directly on the stainless steel surface. During oxidation, a chromia-based layer formed at the interface of the coating and the stainless steel. The chromia layer was initially thicker after oxidation in the non-preoxidized samples than in the preoxidized samples of the same treatment. Presented in Figure 3.1 are coated samples that have not been oxidized. Each sample was preoxidized for a different amount of time from 0 to 100 hours. From left to right, Figure 3.1a was not preoxidized while Figure 3.1b was preoxidized for 3 hours, Figure 3.1c was preoxidized for 10 hours and Figure 3.1d was preoxidized for 100 hours. The lighter gray preoxidation layer can be seen most easily in Figure 3.1d between the alloy and the coating.

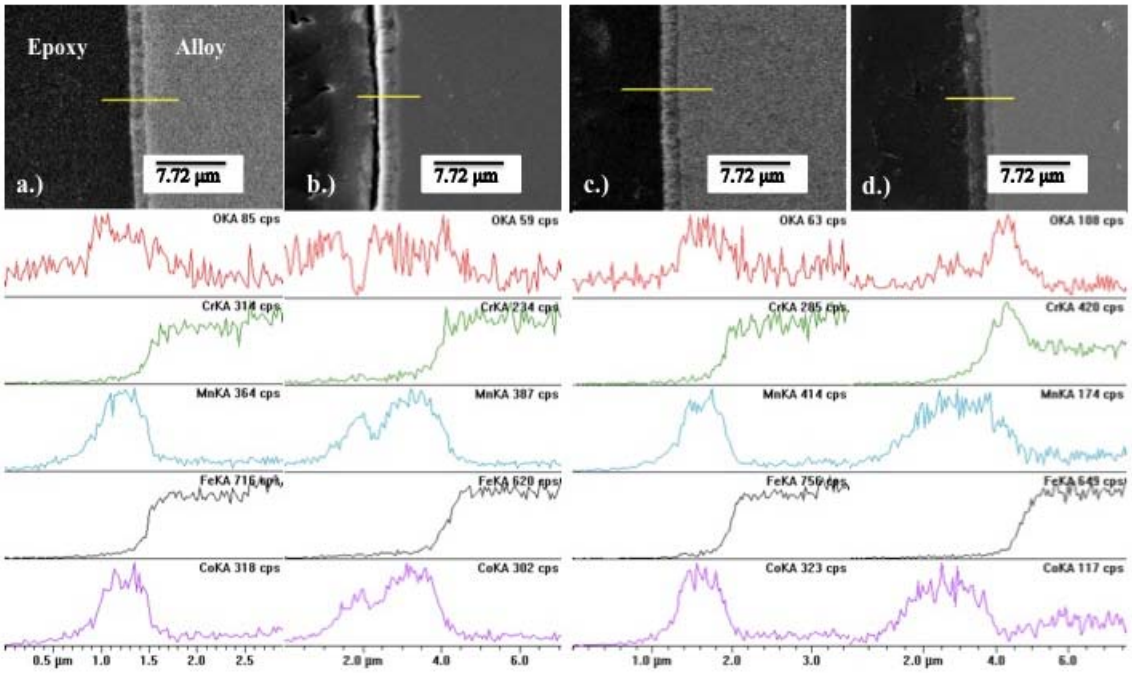


Figure 3.1 Cross section EDS elemental line scans of a.) 0pre-0ox b.) 3pre-0ox c.) 10pre-0ox d.)100pre-0ox

Presented in Figure 3.2 are cross-section EDS elemental line scans of samples after 10 hours of oxidation. The sample shown Figure 3.2a was not preoxidized while samples in Figures 3.2b, 3.2c and 3.2d were each preoxidized for 3 hours, 10 hours and 100 hours, respectively. The surface oxide layer of the non-preoxidized sample, including both the coating and the chromia-based layer, is nearly twice as thick as the preoxidized samples. The surface oxide layer of the preoxidized samples are all about the same thickness.

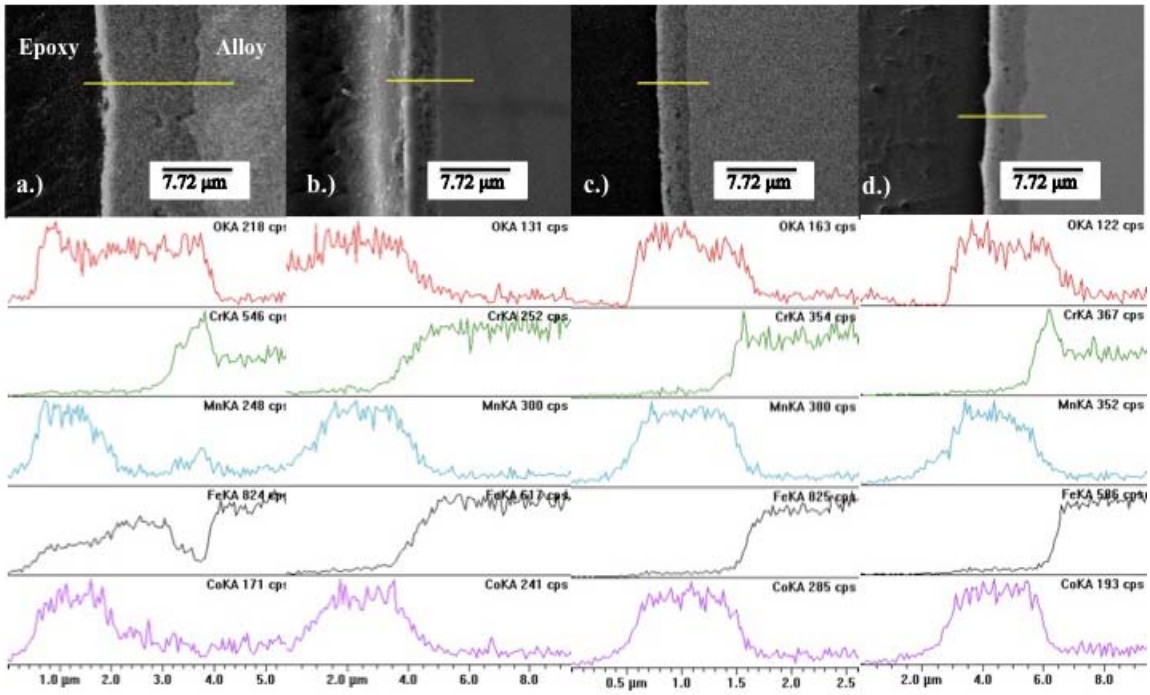


Figure 3.2 Cross section EDS linescans of a.)0pre-10ox b.)3pre-10ox c.) 10pre-10ox d.) 10pre-10ox

Presented in Figure 3.3 are cross-section EDS elemental maps of Cr and Fe from samples after 10 hours of oxidation, each preoxidized for a different time. The sample shown in Figure 3.3a was preoxidized for 0 hours, the sample shown in Figure 3.3b was preoxidized for 3 hours, Figure 3.3c was preoxidized for 10 hours and Figure 3.3d was preoxidized for 100 hours. Fe is present in the coating after 10 hours of oxidation in the non-preoxidized sample. As was also seen in Figure 3.2, preoxidized samples do not exhibit significant Fe presence in the coating after 10 hours of oxidation. The thermally-grown chromia-based layer is thicker in the non-preoxidized sample. In Figure 3.3b (3pre-10ox sample from Table 2.2), Fe does not appear in the coating. The lack of Fe in the coating is consistent with the other preoxidized samples with longer preoxidation times even though the chromia-based layer is not thick enough to be visible in the EDS elemental map.

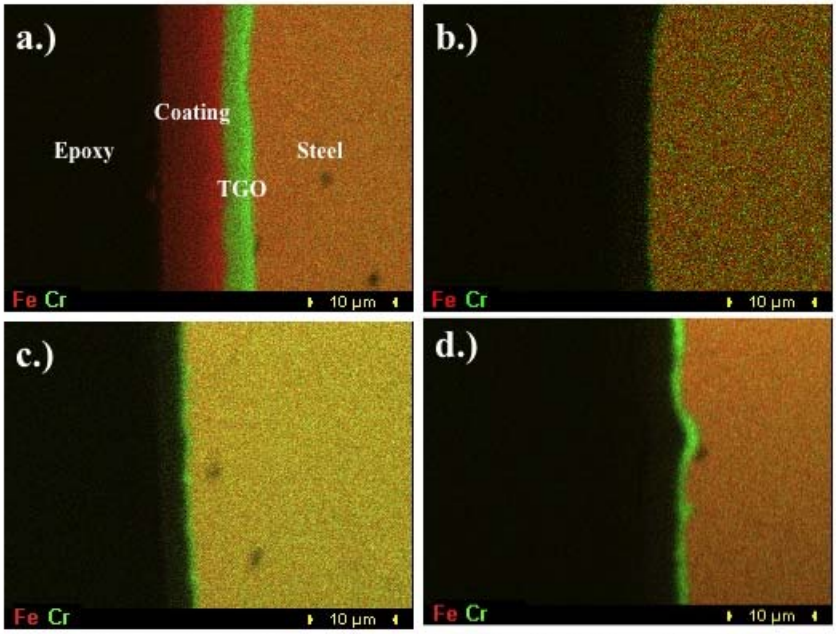


Figure 3.3 Cross section EDS elemental maps of: a.) 0pre-10ox b.) 3pre-10ox c.) 10pre-10ox d.) 100pre-10ox

EDS cross-section elemental line scans presented in Figure 3.4 show samples oxidized for 100 hours. Figure 3.4a, b, c, and d are non-preoxidized, preoxidized for 3 hours, preoxidized for 10 hours and preoxidized for 100 hours respectively. Voids are visible in the surface oxide layers in all samples. The surface oxide layer of the non-preoxidized sample is about three times thickner than the surface oxide layer of the preoxidized samples. All of the surface oxide layers of the preoxidized samples are similar in thickness.

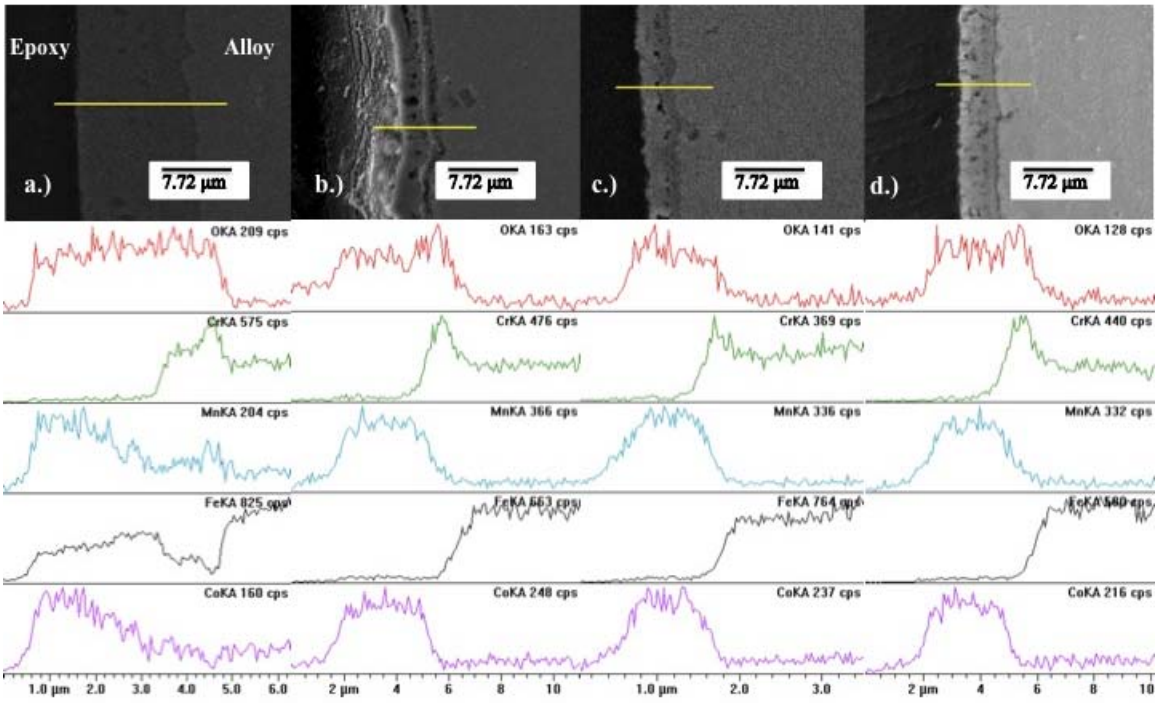


Figure 3.4 Cross section EDS elemental line scan of a.) 0pre-100ox b.) 3pre-100ox c.) 10pre-100ox d.) 100pre-100ox

EDS cross-section elemental maps presented in Figure 3.5 show the presence of Fe and Cr in samples oxidized for 100 hours and preoxidized for 0, 3, 10 or 100 hours in Figures 3.5a, 3.5b, 3.5c, and 3.5d, respectively. The trend observed in Figure 3.5 is consistent with the 10 hours of oxidation samples seen in Figure 3.4, i.e. Fe is present in the coating in only the non-preoxidized sample (0pre-100ox from Table 2.2). Chromia layer thicknesses in these images are similar across all preoxidation levels.

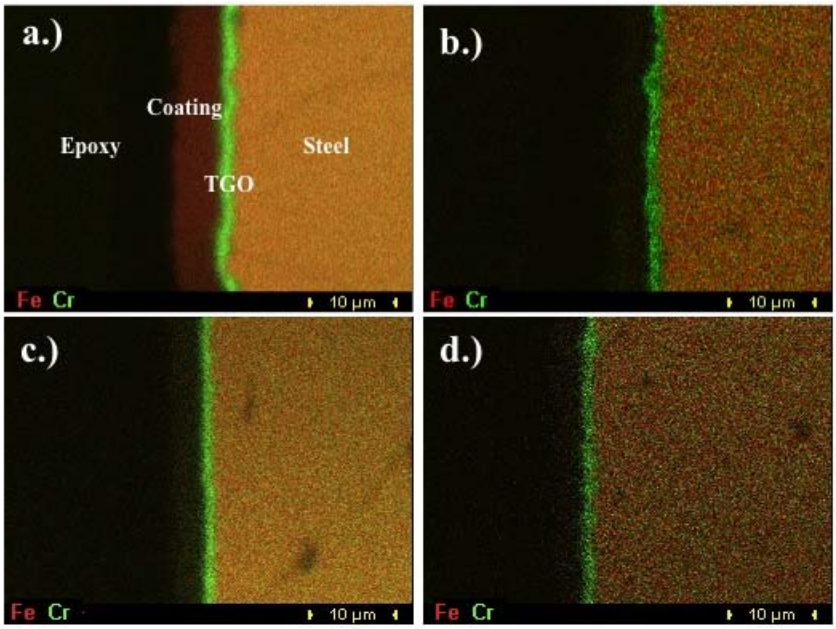


Figure 3.5 Cross section EDS elemental maps of: a.) 0pre-100ox b.) 3pre-100ox c.) 10pre-100ox d.) 100pre-100ox

Presented in Figure 3.6 are cross section EDS line scans of the ASR witness samples after 1650 hours of oxidation. The sample shown in Figure 3.6a was not preoxidized and the sample shown in Figure 3.6b was preoxidized for 100 hours. As in previous images, Fe is not present in the coating of preoxidized sample but is seen in the coating of the non-preoxidized sample. Cr is not visible in the coating line scan of the preoxidized sample shown in Figure 3.6b but is visible in the coating line scan of the non-preoxidized sample shown in Figure 3.6a.

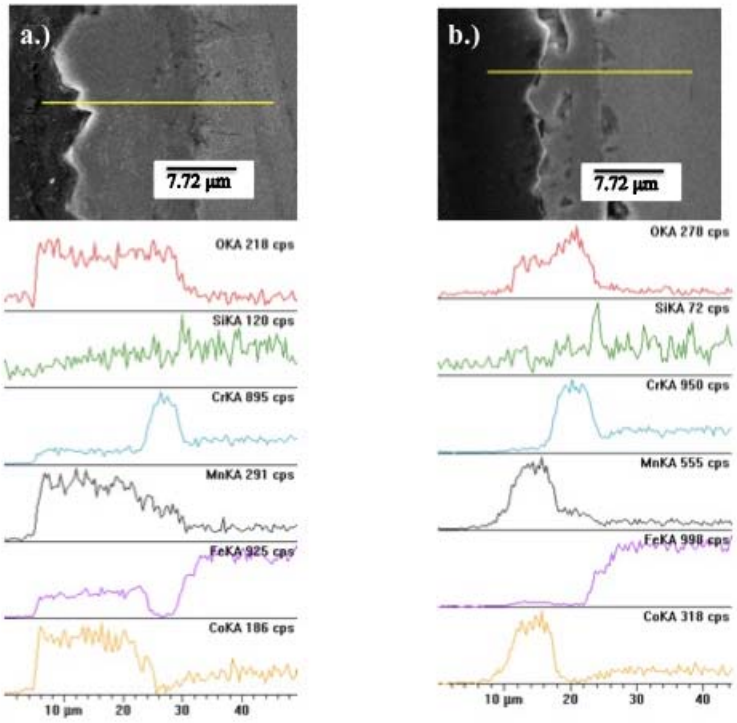


Figure 3.6 Cross section EDS elemental line scans of: a.) 0pre-1650ox b.) 100pre-1650ox

Outward Fe transport occurred into the coating in the non-preoxidized sample. The cross section morphology of the non-preoxidized sample is very homogeneous and uniform from the steel to the gas interface. There are some voids along the alloy-chromia-based layer interface and the chromia-based layer also contains some small voids.

Outward Fe transport did not occur in the preoxidized sample. The cross section morphology of the preoxidized sample includes a distinct separation between the chromia-based layer and the coating. Voids are present in the steel along the oxide interface and in the CoMn spinel layer along the chromia-based layer interface, however no voids are visible in the chromia-based layer itself.

As seen in Figure 3.6 EDS line scans of both sample 0pre-1650ox and sample 100pre-1650ox, some Si is present between the chromia and the steel; however, it is irregular in presence and in thickness, not forming a uniform layer.

Presented in Figure 3.7 are EDS elemental cross-section maps of non-preoxidized and 100 hour preoxidized samples that were oxidized for 1650 hours. Just as in Figures 3.3 and 3.5, only Fe and Cr are displayed and Fe is present in the coating only in the non-preoxidized sample. In Figure 3.7, the chromium-rich layers are nearly the same thickness in both the non-preoxidized and preoxidized samples and range from 3 to 4 μm. After 1650 hours of oxidation, the chromia-based surface layer thickness is variable. Fe and Cr are visible in the coating region of the non-preoxidized sample shown in Figure 3.7a.

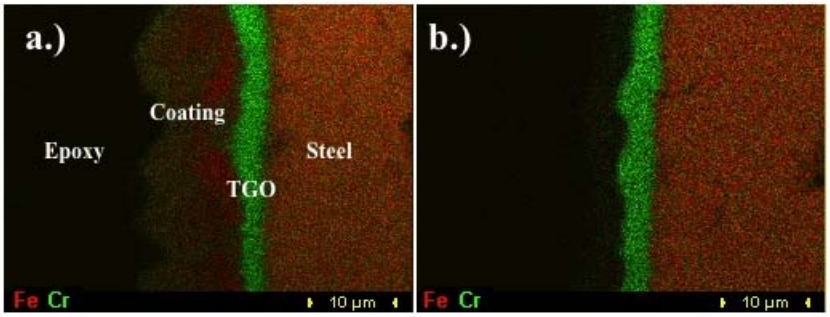


Figure 3.7 Cross section EDS elemental maps of: a.) 0pre-1650ox b.) 100pre-1650ox

Over the course of the oxidation treatment, as seen in Figures 3.1-3.7, Fe was not detected in any of the preoxidized sample coatings after oxidation. Preoxidation levels of 3 hours, 10 hours and 100 hours were all observed to inhibit Fe transport into the coating. In the non-preoxidized samples Fe was detected in the coating. These trends persist over 1650 hours of oxidation in 800°C laboratory air. The effects of preoxidation to form an

Fe transport barrier and maintaining a thinner coating are manifested in as little as 3 hours of preoxidation at 800°C in air.

Surface Morphology

Figure 3.8 presents micrographs of 0 hour oxidized samples and the sample in Figure 3.8a was non-preoxidized, the sample in Figure 3.8b was preoxidized for 3 hours, the sample in Figure 3.8c was preoxidized for 10 hours and the sample in Figure 3.8d was preoxidized for 100 hours. The coatings are amorphous and globular without facets. No crystals have formed at this stage. The samples in Figures 3.8a and 3.8b have less globular coatings than the samples in Figures 3.8c and 3.8d.

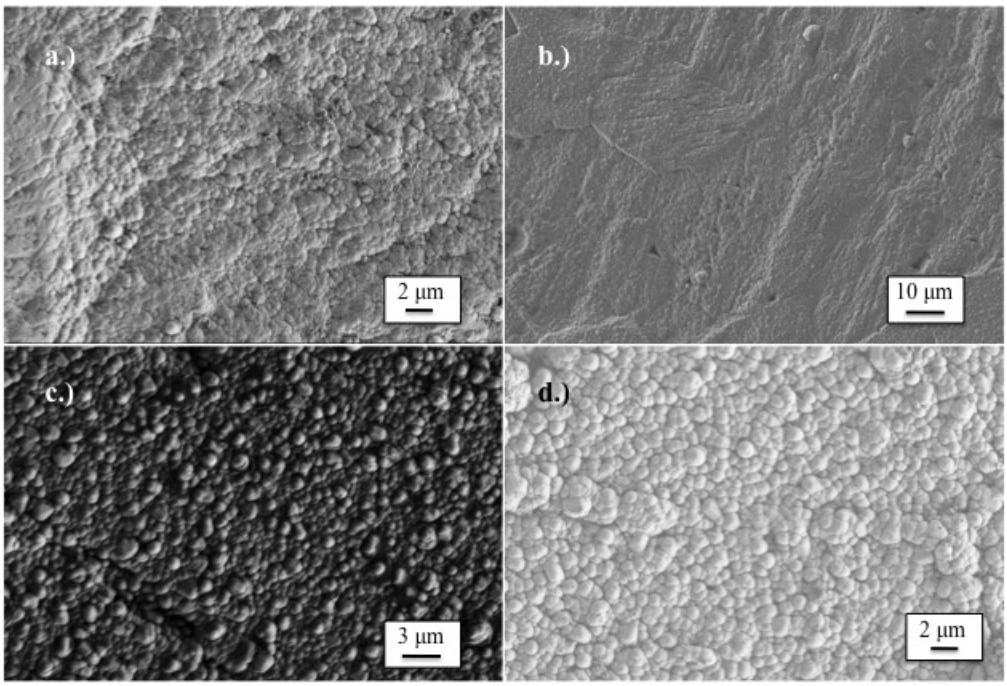


Figure 3.8 Micrographs of coating surface of: a.)0pre-0ox b.) 3pre-0ox c.) 10pre-0ox d.) 10opre-0ox

Figure 3.9 presents micrographs of the coating surfaces after 10 hours of oxidation for both preoxidized and non-preoxidized samples. After 10 hours of

oxidation, the non-preoxidized sample in Figure 3.9a shows pores in the coating and the preoxidized samples do not show pores. All of the coatings appear crystalline and the crystals on the non-preoxidized sample are slightly bigger.

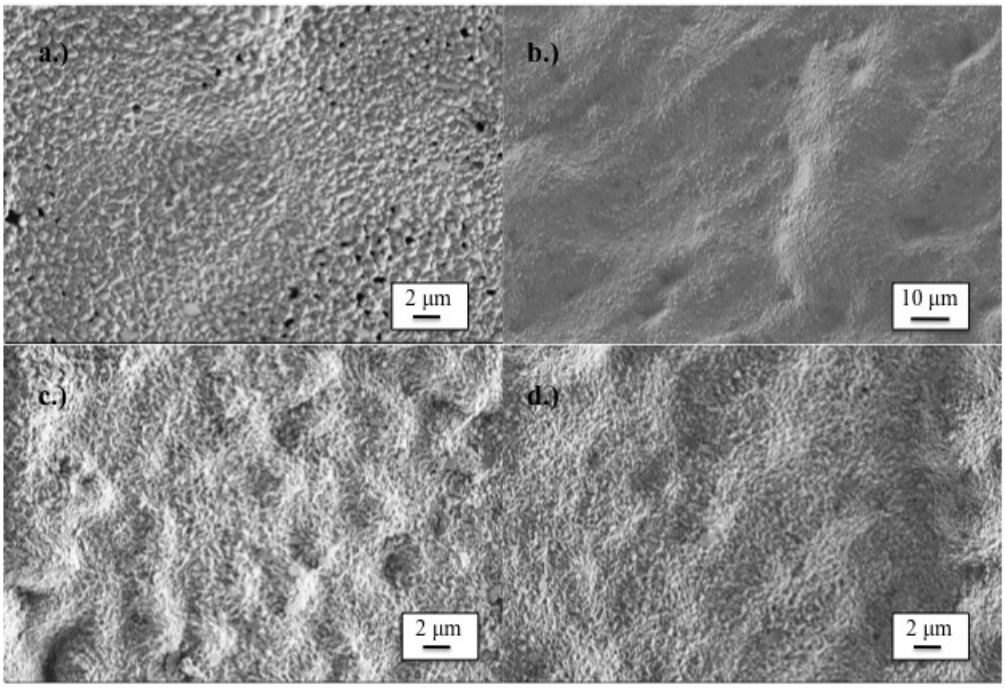


Figure 3.9 Micrographs of coating surface of: a.)0pre-10ox b.) 3pre-10ox c.) 10pre-10ox d.) 100pre-10ox

Figure 3.10 shows micrographs of the coating surfaces after 100 hours oxidation. Pores are still visible in only the non-preoxidized sample. The crystals are more globular and uniform in size in the non-preoxidized sample. In the preoxidized samples the crystals are more variable in size.

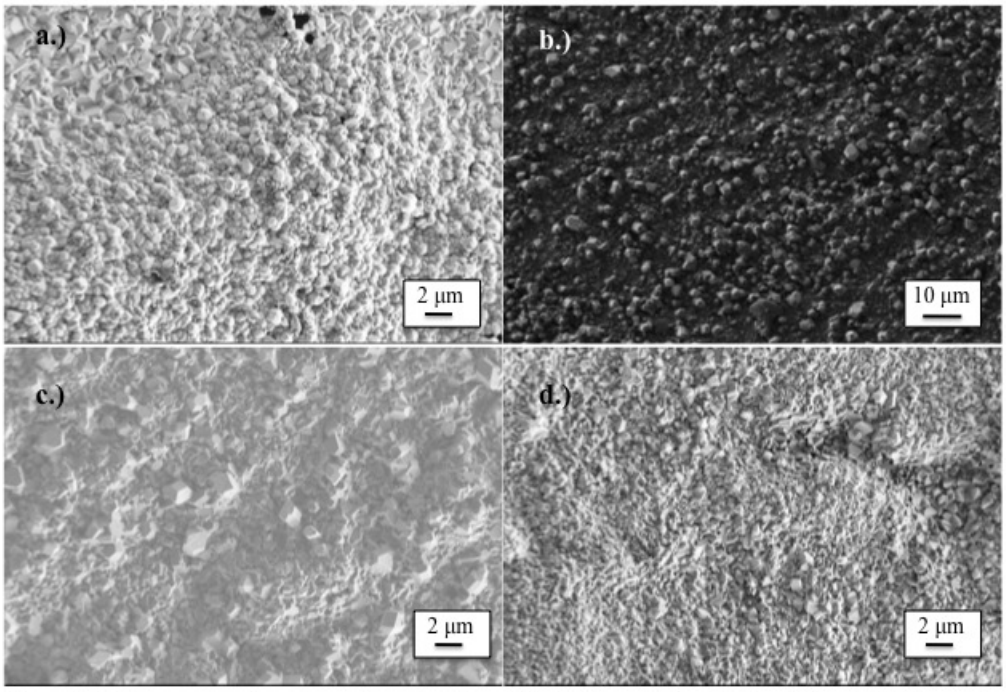


Figure 3.10 Micrographs of coating surface of: a.)0pre-100ox b.) 3pre-100ox c.) 10pre-100ox d.) 100pre-100ox

Figure 3.11 presents scanning electron micrographs of sample 0pre-1650ox. The surface composition is uniformly Co, Mn and Fe in the non-preoxidized sample, 0pre-1650ox. The coating morphology is not uniform in appearance with many small crystals and a few large crystals with the appearance of grains.

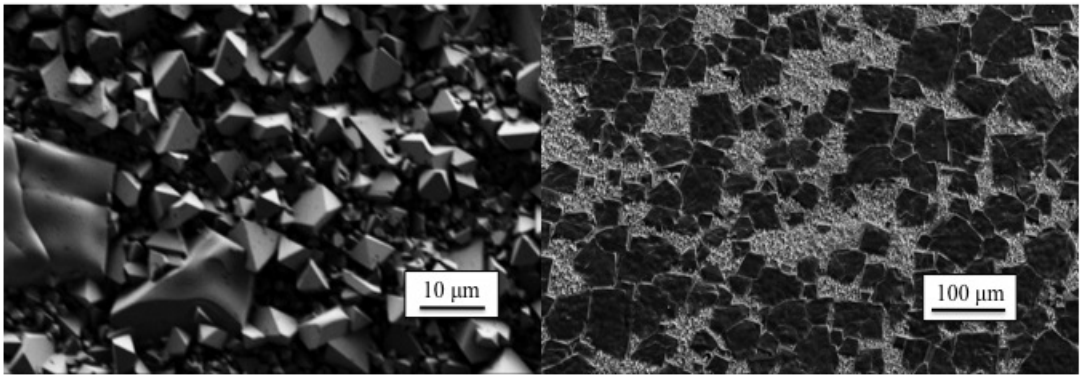


Figure 3.11 Scanning electron micrographs of 0pre-1650ox

Figure 3.12 presents scanning electron micrographs of sample 100pre-1650ox. The surface composition is uniformly Co and Mn in the preoxidized sample, 100pre-1650ox. The coating morphology is uniform in appearance with many small crystals.

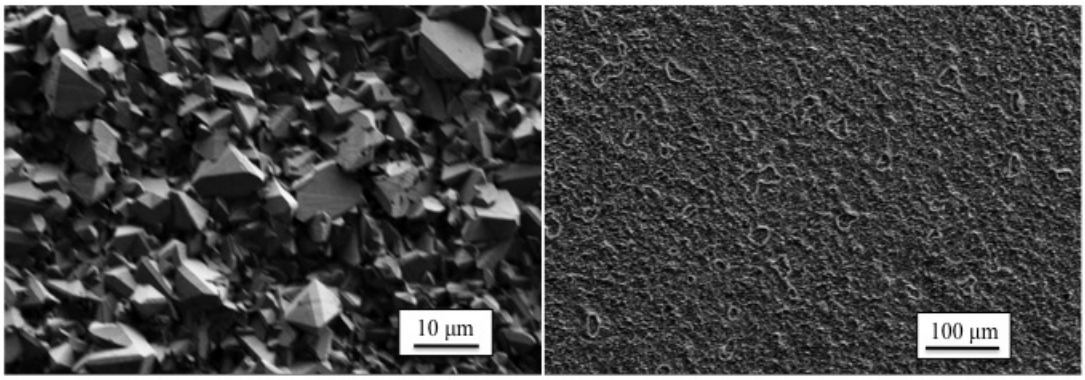


Figure 3.12 Scanning electron micrographs of 100pre-1650ox

Coating Deposition Investigation

Presented in Figure 3.13 are the EDS elemental line scans of two non-preoxidized samples and a preoxidized sample that have been oxidized for 10 hours. Figure 3.13a shows a sample coated with CoMn in an oxygen atmosphere causing the coating to be deposited as an oxide. Figure 3.13b shows a sample coated with CoMn in a low pressure Ar atmosphere causing the coating to be deposited as a metal. Figure 3.13c shows a 10 hour preoxidized sample with a metal deposited coating. The sample coating in Figure 3.13a is extremely fragile so the crack is most likely an artifact of polishing. Oxide deposited $(CoMn)_3O_4$ coatings were very fragile and unable to withstand cross sectioning and polishing after oxidation times of longer than 10 hours.

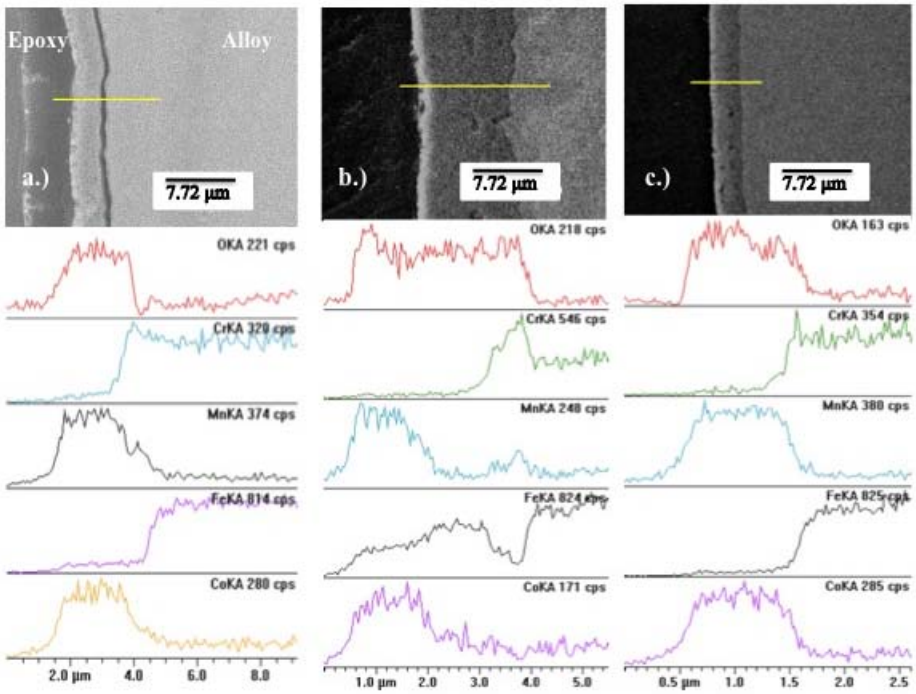


Figure 3.13 Cross sections EDS line scans of: a.) 0pre-10ox-Ox b.) 0pre-10ox-Met c.) 10pre-10ox

A small amount of Fe appeared to have transported into the coating in the oxide-coated sample 0pre-10ox-Ox shown in Figure 3.13a. The greatest amount of Fe transport was observed into the non-preoxidized metal deposited coating of sample 0pre-10ox-Met (as listed in Table 2.2) as shown in Figure 3.13b. The least amount of Fe transport is observed in the preoxidized 10pre-10ox sample as shown in Figure 3.13c.

Presented in Figure 3.14 is a TOF-SIMS sputtered depth profile for a non-preoxidized sample with an oxide deposited CoMnO coating that was oxidized for 10 hours. Higher sputter times along the x axis correspond to deeper into the coating, closer to the stainless steel interface. Due to the matrix effect, the magnitudes of the counts do not deliver quantitative composition information and vary between materials. The magnitudes can be compared for one element in similar materials across samples. The magnitude of Fe is on the order of 1200 in the oxide coating section in Figure 3.14.

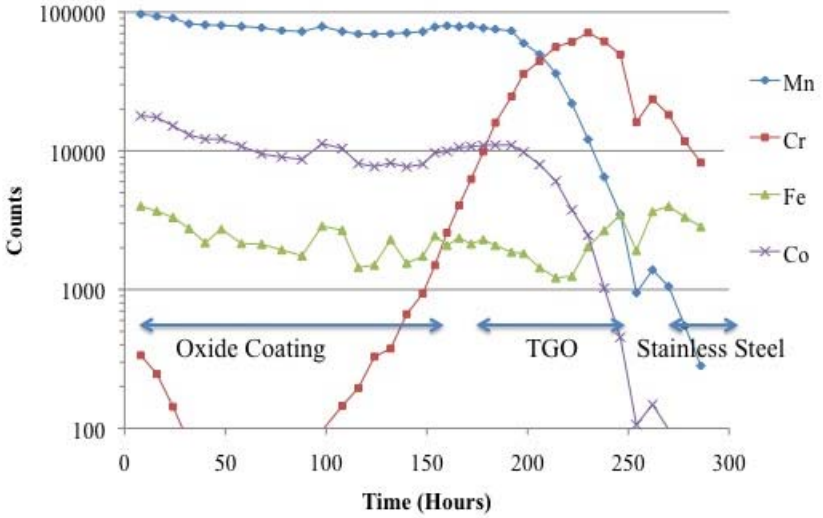


Figure 3.14 TOF-SIMS sputtered depth profiles for 0pre-10ox-Ox

Presented in Figure 3.15 is the TOF-SIMS sputtered depth profile for the non-preoxidized sample that was coated with CoMn metal and oxidized for 10 hours. The magnitude of Fe is on the order of 100,000 in the oxide coating section of Figure 3.15.

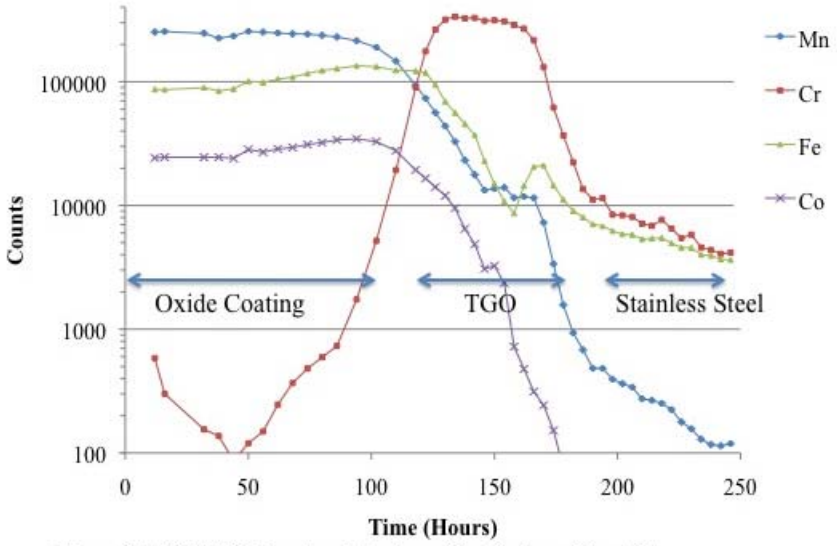


Figure 3.15 TOF-SIMS sputtered depth profiles for 0pre-10ox-Met

Presented in Figure 3.16 is a TOF-SIMS sputtered depth profile of a sample preoxidized for 10 hours, coated with CoMn metal and oxidized for 10 hours. The magnitude of Fe is about 10,000 in the region of the oxide coating.

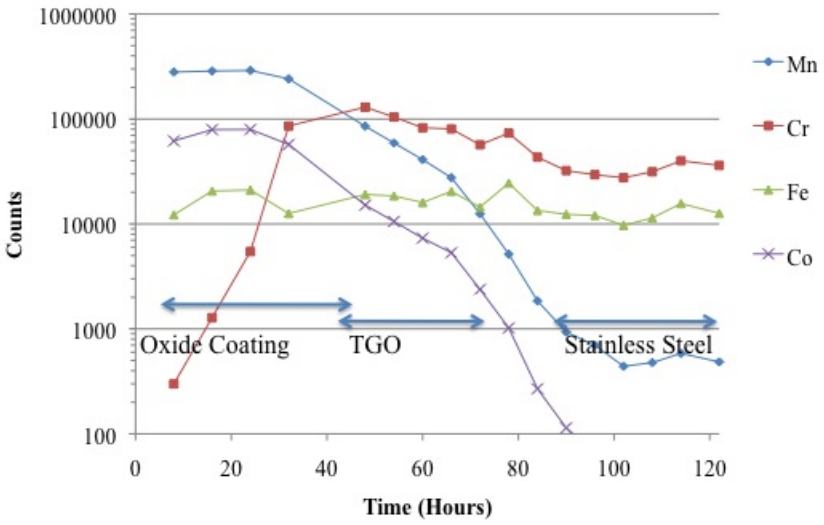


Figure 3.16 TOF-SIMS sputtered depth profiles for 10pre-10ox

The TOF- SIMS sputtered depth profiles for metal-deposited coatings are consistent with the EDS line scans in Figure 3.13. They show with high resolution that Fe transports significantly into the non-preoxidized sample and transports an order of magnitude less into the coating of the preoxidized sample. The oxide deposited coating shows results that conflict with EDS results and this can be attributed to the poor oxide cohesion, hardness and mixing during the sputtering process.

Phase Development

Presented in Figure 3.17 are XRD patterns of samples oxidized for 0 hours. Phases correspond to the shapes listed in the legend. The green pattern shows strong peaks at about 42 and 45 degrees that are characteristic of the body-centered cubic ferritic

stainless steel substrate. The Cr_2O_3 phase (eskolaite) is present on all samples prior to oxidation, including the stainless steel substrate. The coating is deposited as an amorphous metal mixture, which is characterized by the broad bump at low angles and the lack of peaks.

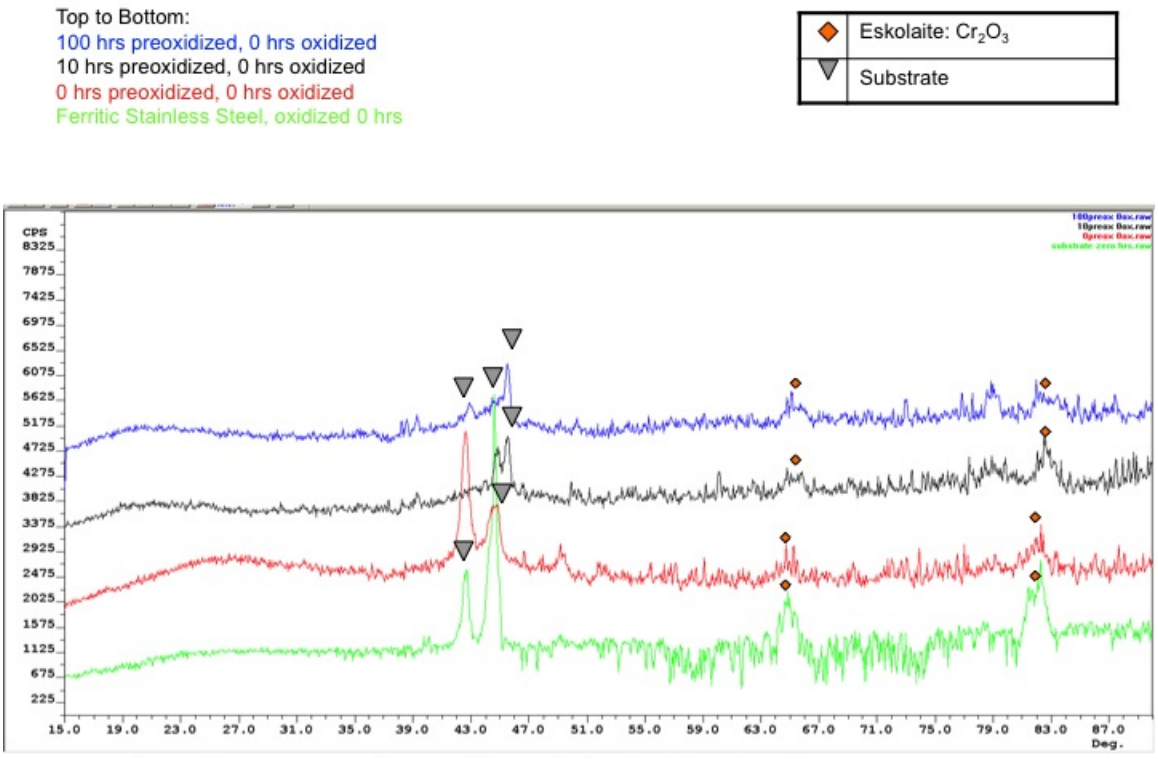


Figure 3.17 XRD patterns of: Bare stainless steel, 0pre-0ox, 10pre-0ox, 100pre-0ox

Presented in Figure 3.18 are XRD patterns for samples oxidized for 10 hours. The same substrate peaks are present as in the samples shown in Figure 3.17. The Cr_2O_3 (eskolaite) peaks are larger in all four samples. The spinel peaks are visible in all three coated samples but not the bare stainless steel. Some small peaks are also visible indicating the presence of other trace phases.

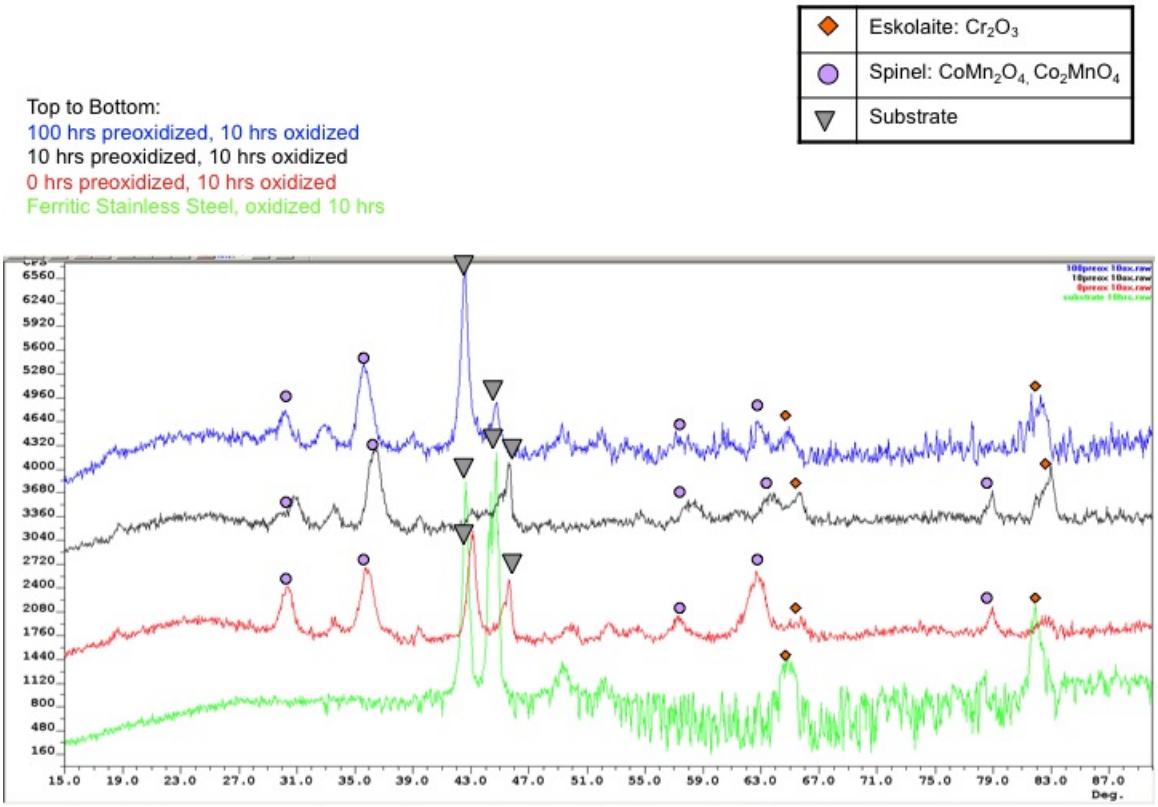


Figure 3.18 XRD patterns of: Bare stainless steel oxidized for 10 hours, 0pre-10ox, 10pre-10ox, 100pre-10ox

Presented in Figure 3.19 are XRD patterns for samples oxidized for 100 hours. The same substrate peaks are present as in the samples oxidized for 0 and 10 hours. The Cr_2O_3 (eskolaite) and spinel heights are about the same magnitude as in Figure 3.18. Eskolaite is still present in the preoxidized samples after 100 hours of oxidation however only a very small amount of eskolaite is present in the non-preoxidized sample after 100 hours of oxidation.

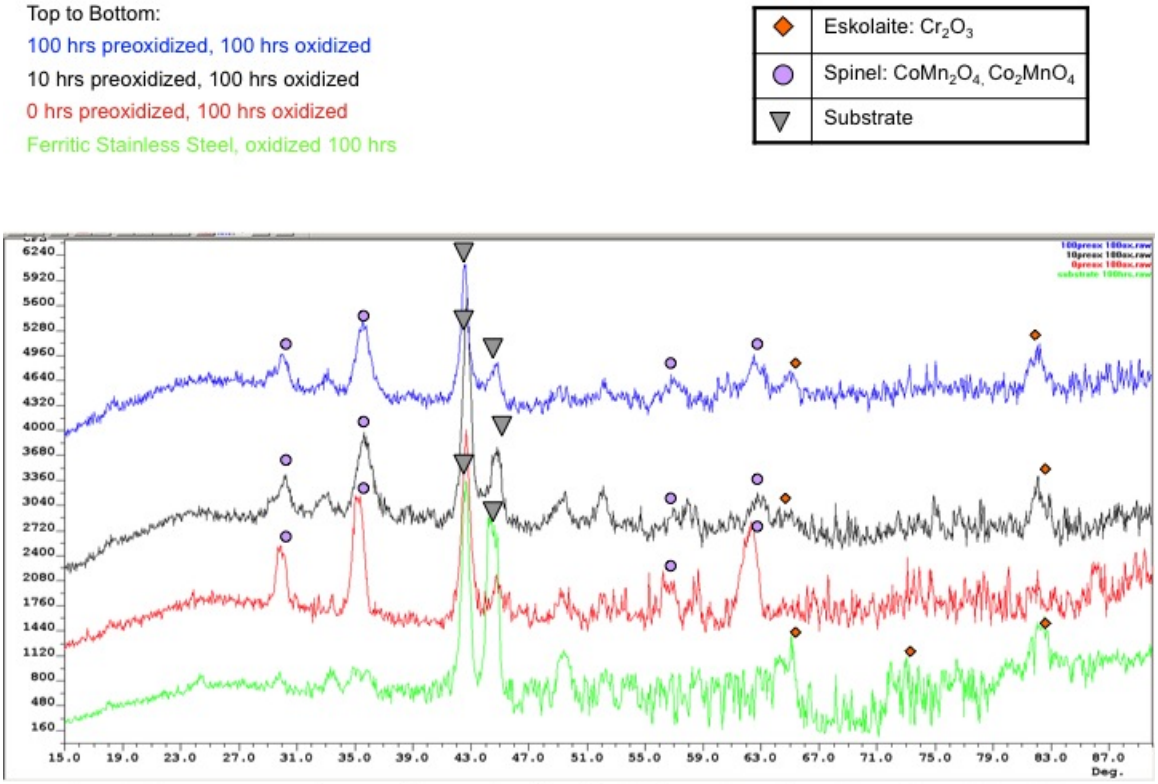


Figure 3.19 XRD patterns of: Bare stainless steel oxidized for 100 hours, 0pre-100ox, 10pre-100ox, 100pre-100ox

Thermogravimetric Analysis

The mass gain curves from a thermogravimetric analysis are shown in Figure 3.20. The preoxidized samples consistently gain less mass per unit time than non-preoxidized samples. In Figure 3.20b, the parabolic rate constant of the preoxidized sample is shown to be 3 x 10^{-4} $mg^2cm^{-4}ks^{-1}$ and the parabolic rate constant of the non-preoxidized sample is shown to be 4 x 10^{-4} $mg^2cm^{-4}ks^{-1}$. P-tests found the slope constants for both of the sample series to be statistically significant and the intercept constants for both of the sample series to be statistically insignificant.

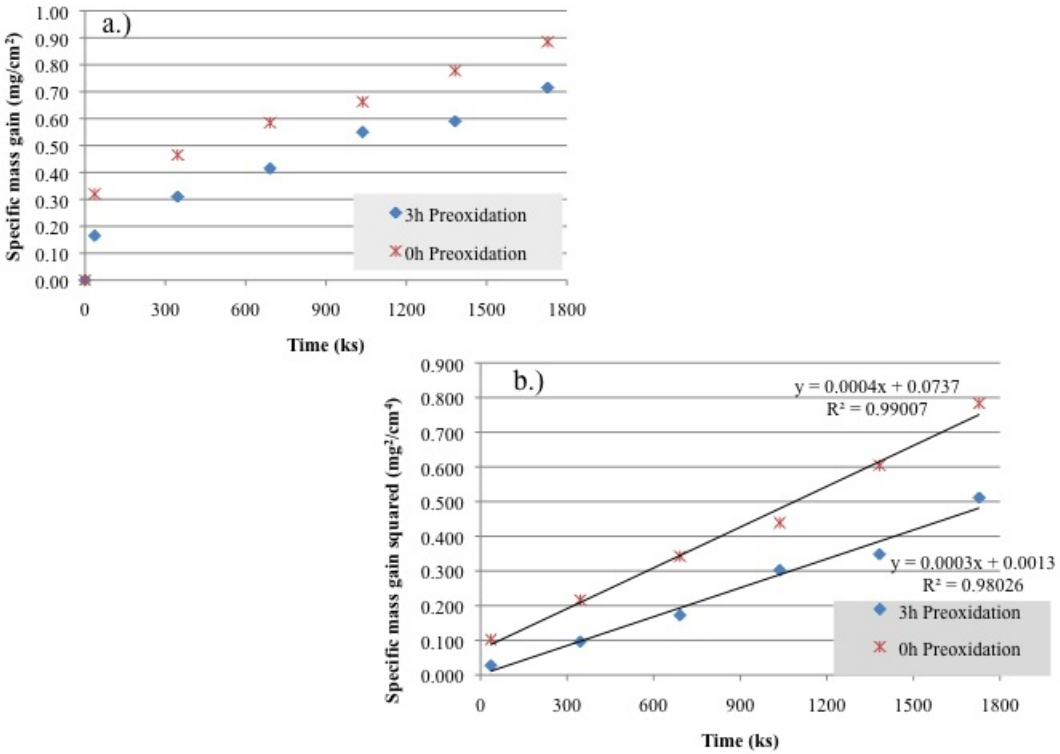


Figure 3.20 Thermogravimetric Analysis of samples preoxidized for 0 or 3 hours a.) Specific mass gain v. time b.) Specific mass gain squared v. time, with linear regression

Dual Atmosphere

Presented in Figure 3.21 are the EDS elemental line scans for the moist dual atmosphere exposed samples. Figure 3.21a was non-preoxidized and Figure 3.21b was preoxidized for 3 hours. As with laboratory air exposures, a thicker surface oxide layer and Fe transport into the coating were visible in non-preoxidized sample after 300 hours of dual atmosphere exposure. A thinner surface oxide layer and very minimal Fe transport into the coating occurred in the preoxidized sample. Many voids formed in the surface oxide layer and some chromium is visible on the outer surface of the coating in both dual atmosphere samples. A small amount of Cr is observed within the coating.

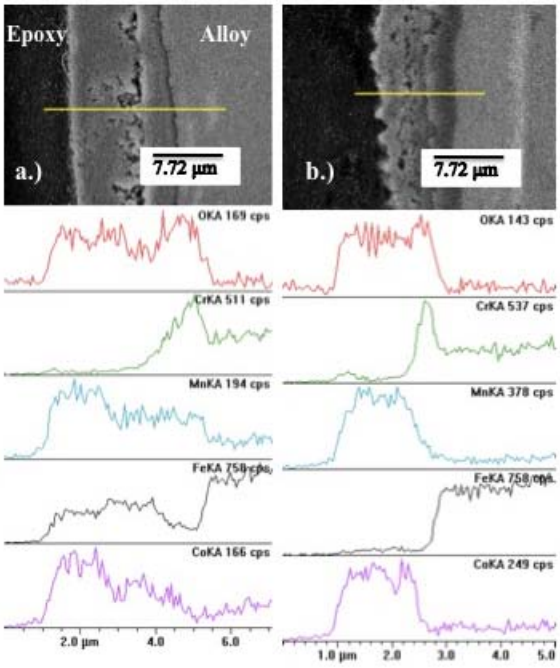


Figure 3.21 Cross section EDS elemental line scans of: a.) 0pre-Dual b.) 3pre-Dual

Presented in Figure 3.22 are the EDS elemental line scans for the moist air-air exposed samples. Figure 3.22a was non-preoxidized and Figure 3.22b was preoxidized for 3 hours. The surface oxide layer of the non-preoxidized sample was only slightly thicker than that of the preoxidized sample. Fe transported into the coating of the non-preoxidized sample but less than in sample 0pre-Dual (from Table 2.2) shown in Figure 3.21a. Minimal Fe transported into the preoxidized sample. Just as in the dual atmosphere sample, many voids formed in the surface oxide layer and some chromium is detected on the outer surface of the coating of both air-air atmosphere samples but not throughout the coating.

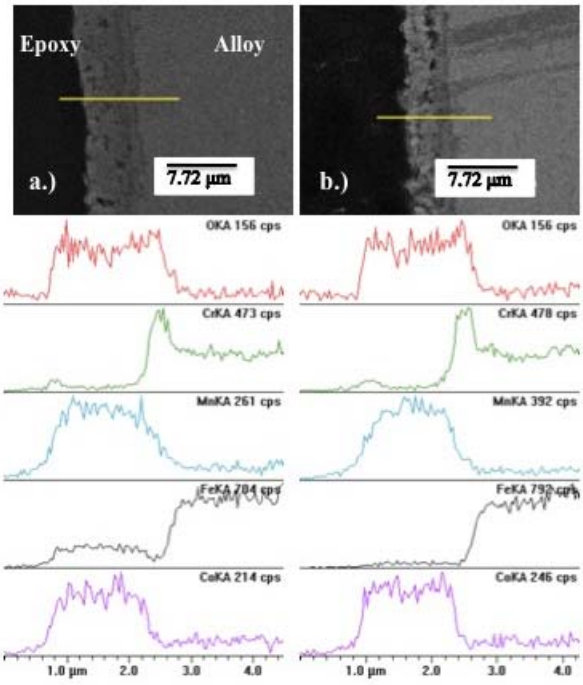


Figure 3.22 Cross section EDS elemental line scans of: a.) 0pre-Air b.) 3pre-Air

Area Specific Resistance

ASR data of 100 hours preoxidized and non-preoxidized samples in 800°C are presented in Figure 3.23. During the first 1400 hours, the ASR values of the two samples are very similar. During the last 200 hours, the ASR values begin to exhibit different trends. The ASR of the preoxidized sample slightly decreases and the ASR of the non-preoxidized sample increases. At 1650 hours the ASR of the preoxidized samples was ~4 $m\Omega \cdot cm^2$ and the ASR of the non-preoxidized sample was ~5 $m\Omega \cdot cm^2$.

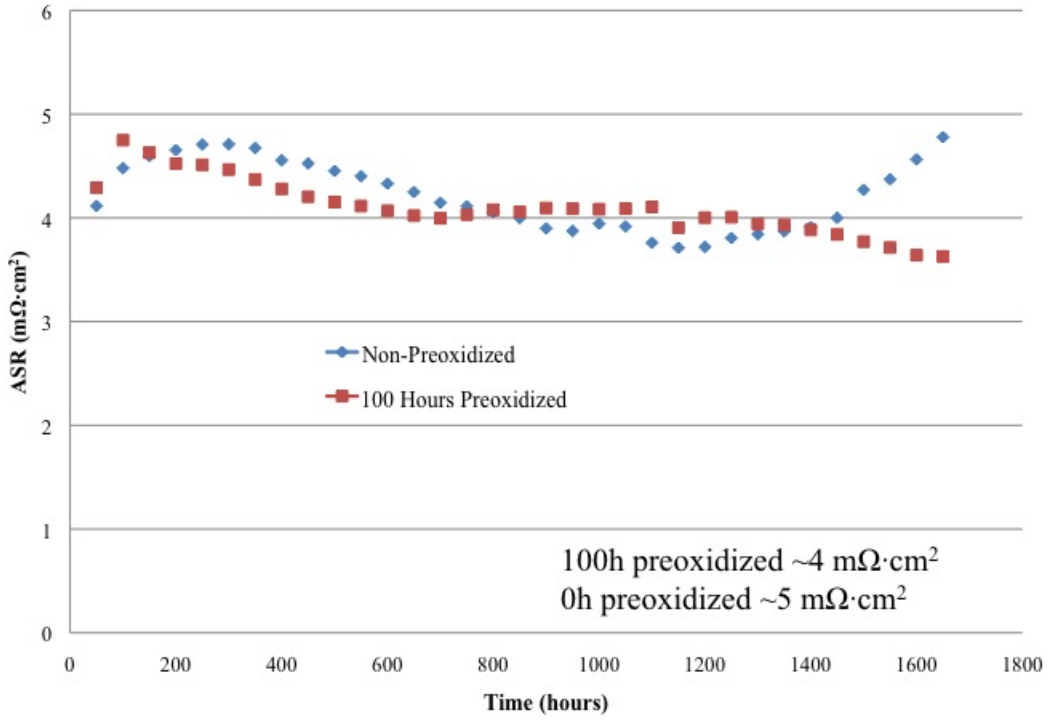


Figure 3.23 Area Specific Resistance test with platinum connection paste at 800°C.

Adhesion

Figure 3.24 presents optical microscope images of sample surfaces subsequent Rockwell C Indentation that show the adhesion behavior of the coating and chromia-based layer. Dark areas around the indentation indicate delamination of the coating. Gray areas around the indentation indicate delamination of both the coating and the chromia-based layer. Delamination implies poor adhesion or interfacial fracture toughness [27]. In these qualitative adhesion tests, the non-preoxidized sample coatings appeared better adhered to the stainless steel substrate over 100 hours of oxidation than the preoxidized samples. In the preoxidized samples, at early oxidation times, the coating delaminated while the chromia-based layer remained attached. In the preoxidized samples, the coating as well as the chromia-based layer delaminated after longer oxidation times. The

chromia-based layer and coating that were least well adhered were the 3 hour preoxidized sample series.

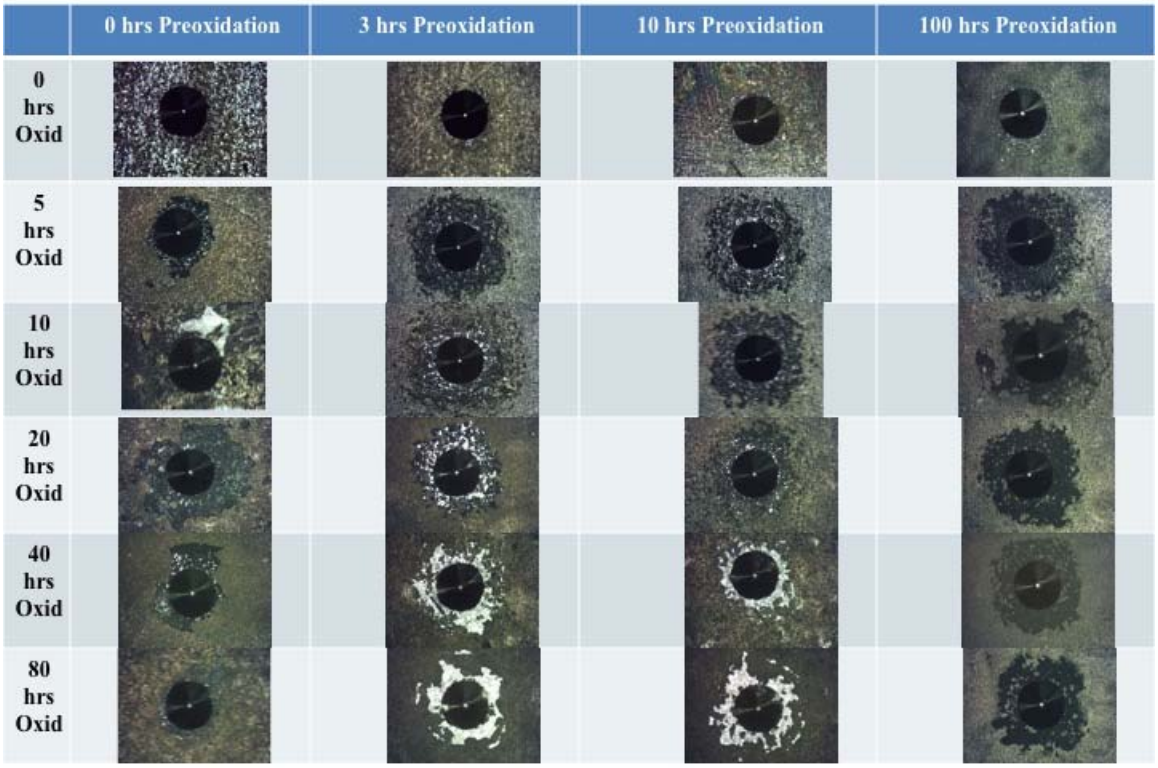


Figure 3.24 Optical microscope images of Rockwell Indenter Adhesion Test

CHAPTER 4

DISCUSSION

Elemental Transport and Thickness

Presented in Figure 4.1 is a cartoon of the oxidation behavior findings. The three types of coatings deposited are preoxidized metal deposited for various levels, non-preoxidized metal deposited and non-preoxidized oxide deposited coatings. Each resulted in different oxidation behavior with respect to thickness, composition and microstructure.

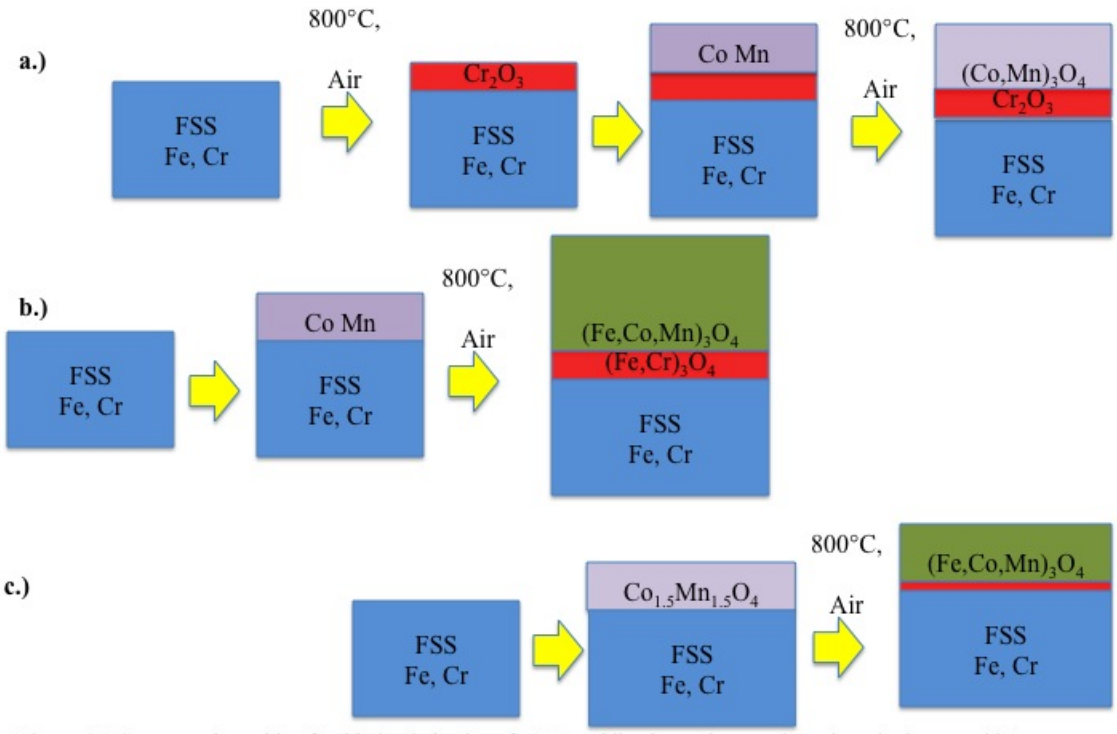


Figure 4.1 Conceptual graphic of oxidation behavior of a.) Preoxidized samples, coatings deposited as metal b.) non-preoxidized samples, coatings deposited as metal c.) non-preoxidized samples, coatings deposited as oxide.

In the non-preoxidized coated samples, both Fe and Cr transport outward from the stainless steel toward the high p_{O2} air interface. Then, the Cr forms the chromium-based layer while the Fe becomes part of the coating. Fe transport into the coating of non-preoxidized samples has also been observed in other $(Co,Mn)_3O_4$ coatings on non-preoxidized stainless steel substrates [34-36]. Without a coating, Fe oxides are known to form in addition to chromium oxides due to a negative Gibbs free energy of formation [29].

The thicker chromia-based layer observed in the non-preoxidized samples may be the result of the presence of Fe oxides in the outer coating layer. The Fe oxides seem to create a surface oxide layer more permeable to oxygen causing oxygen to continue to diffuse inward so that the Cr-rich layer continues to grow [35]. In the preoxidized samples, where no Fe oxides were present in the coating, the $(Co,Mn)_3O_4$ does not seem to facilitate as much inward oxygen transport, limiting further growth of the chromia-based layer. To benefit the SOFC interconnect, less interfacial stresses and less thickness across which electrons have to flow is beneficial, and can be obtained by preoxidizing stainless steel prior to coating.

A likely mechanism to explain the Fe transport into the non-preoxidized coatings could arise from the initial metal-metal interface. The metal-metal interface may allow for small amounts of interfacial alloying during early stages of oxidation. The Fe seems to be most diffusive in metallic CoMn.

Qualitatively, from the EDX elemental composition maps Fe concentration does not seem to increase in the coating over time. This implies that Fe doesn't continue to

transport into the coating in non-preoxidized samples after the initial stages of oxidation. In later stages of oxidation the chromia-based layer may block Fe transport or the oxidized Co and Mn species may also be less diffusive to Fe cations. From the relative amounts of Fe transport in the various coatings, it seems that Fe is most permeable in CoMn metal, less permeable in CoMn oxides, and Fe is minimally permeable in chromia.

The preoxidation layer forms in a high p_{O2} atmosphere relative to chromium oxidation after coating deposition. Chromia in a high p_{O2} atmosphere behaves as a metal excess n-type oxide with transport being dominated by cations moving toward the gas interface. Chromia in a low p_{O2} atmosphere (coated metal during oxidation) behaves as a metal-deficit p-type oxide where cations still move toward the gas interface. This implies that chromia is never the anion-deficient n-type conductor in which O anions would diffuse through the chromia to the steel. As a result chromia typically forms at the oxide-gas interface. Also, after chromia is formed and coated, preoxidized and non-preoxidized samples alike would behave as a low p_{O2} p-type semiconductor with dominating outward electron and cation transport.

In non-preoxidized samples, since the chromia layer continues to grow, it seems the O anions are more diffusive in Fe, Co, and Mn oxides relative to only Co and Mn oxides.

Surface Morphology

The non-preoxidized samples contain more pores on the surface than the preoxidized samples after oxidation takes place. In the non-preoxidized samples, the presence of pores may correlate with greater outward cation transport as well as the faster oxidation rate that seems to result in thicker coatings. The pores may enable greater inward oxygen anion transport that increases the oxidation rate of the Cr in the stainless steel at the alloy interface resulting in thicker coatings.

The coatings of the preoxidized samples that do not contain visible pores on the surface may not be as permeable to inward oxygen transport, therefore resulting in thinner coatings and a slower oxidation rate. Surface porosity and the governing mechanisms should be investigated further.

Coating Deposition Investigation

To further understand the mechanism for Fe transport and coating thickness, non-preoxidized samples with oxide deposited coatings were analyzed. Slightly more Fe transports into initially deposited $Co_{1.5}Mn_{1.5}O_4$ than into preoxidized metal deposited coatings but less than into non-preoxidized metal deposited coatings. After 10 hours of oxidation, the chromia-based layer under the coatings deposited as $Co_{1.5}Mn_{1.5}O_4$ did not seem to grow to be as thick as the chromia layer in the non-preoxidized metal deposited samples. This may be because the oxygen is less diffusive into $Co_{1.5}Mn_{1.5}O_4$ than into Co, Mn, and Fe oxides [35]. Generally, from Figure 3.13, it seems that $(Co,Mn)_3O_4$ coatings without significant Fe content maintain thinner chromia-based layers.

Due to the fragility of the oxide deposited coatings, TOF-SIMS was also employed. Comparing the Fe counts in the oxide coating across the samples confirms the dramatic difference of Fe diffusivity into the different types of coatings.

Phase Development

At the early oxidation time of 10 hours, both spinel and eskolaite are visible in all three coated samples. After 100 hours of oxidation, the preoxidized and non-preoxidized samples become distinguishable. After 100 hours of oxidation, it seems that the preoxidized samples are still made of two phases, a Cr_2O_3 (eskolaite) sublayer as well as the spinel coating that is expected to be $(CoMn)_3O_4$.

The XRD pattern of the non-preoxidized sample, after 100 hours of oxidation, shows only spinel peaks and the eskolaite phase (chromia) is not visible. Both layers are probably spinel phase and if accompanying EDS information is considered, it can be deduced that $(Fe,Cr)_3O_4$ is the sublayer and $(Co,Mn,Fe)_3O_4$ is the top layer.

Thermogravimetric Analysis

The thermogravimetric analysis results support the findings of thinner coatings of the preoxidized samples relative to the non-preoxidized samples. Preoxidation seems to slow the oxidation growth rate which results in a thinner coating. Faster oxidation rates in the non-preoxidized coatings seem to be a result of the presence of Fe in the coating in addition to Co and Mn oxides. Oxygen transports from the gas phase inward to the chromia interface more easily when Fe oxides are present [35].

The rate constant of the preoxidized sample series is 3 x 10^{-4} $mg^2cm^{-4}ks^{-1}$ and the rate constant of the non-preoxidized sample series is 4 x 10^{-4} $mg^2cm^{-4}ks^{-1}$. The y-axis intercept value has been correlated to the initial oxide scale present before high temperature exposure [26]. In this case the initial oxide layer was established deliberately in the preoxidation step and was shown to be statistically insignificant using the p-test. The steep slope of the oxidation rate that occurs in the first 10 hours is most likely due to the initial deposition of the CoMn coating as a metal and the subsequent oxidation of the CoMn. After the first 10 hours, the Cr in the stainless steel is oxidized. The continued oxidation reaction is diffusion-limited because of the transport of oxygen anions across the coating to meet the Cr cations at the chromia-based layer and coating interface. A good fit of a linear regression to the squared mass gain data as shown in Figure 3.20b shows that the oxidation follows the parabolic rate law.

These TGA results are limited by the short time time-span and the ex-situ method. Each sample sees one ramping up from room temperature and one cooling back down to room temperature. Ideally, the experiment would be in-situ and continued to include data for at least 1000 hours of oxidation.

Dual Atmosphere

Preoxidation influenced dual atmosphere behavior by inhibiting Fe transport and maintaining a thinner surface oxide layer in the preoxidized sample relative to the non-preoxidized sample. It is known that dual atmosphere exposures enhance Fe transport into TGO [37]. This occurs because of the hydrogen (proton) transport through the steel

toward the air-side, which increases the concentration of cation vacancies that may enhance the solubility of Fe and in addition Cr cations [38]. These cation vacancies are created by the protons binding with oxygen anions to form substitutional hydroxide point defects. For metal deficient p-type oxides, as chromia is often considered to be, these can be described with

$$[h^{\cdot}] + [(OH)_O^{\cdot}] = 3[V_M'''']$$

where the concentration of electron holes ($h^{\cdot}$) and the concentration of hydroxide ions (OH) in anion positions of the crystal lattice imply metal vacancies (V_M'''') of the crystal lattice to maintain electroneutrality [37]. More metal vacancies may increase solubility of other cations into the oxide.

Moisture content also encourages Fe transport [29, 14]. Protons dissolved in metal can be represented as either $H_i\cdot$ which describes a proton in an interstitial site or $OH_O^{\cdot}$ which describes a substitutional hydroxide point defect at an oxygen position in the crystal lattice. Outward chromia formation can generally be described with first the consideration of vacancies at the gas interface where the chromia will form and the corresponding ionized oxygen and Cr vacancy [14]

$$[4V_{Cr}'''' + 6V_O^{\cdot\cdot}] + 3O_2 = 6O_O^X + 4V_{Cr}'''' + 12h\cdot$$

Then Cr fills the Cr vacancies and the electron holes move toward the alloy interface,

$$4Cr_{metal} + 6O_O^X + 4V_{Cr}'''' + 12h\cdot = 4Cr_{Cr}^X + 6O_O^X$$

to form chromia [14]. If protons are present, the reaction may change to include the substitutional hydroxide defect and Fe from the metal incorporating into the oxide [14]:

$$6Fe_{metal} + 6OH_O^{\cdot} + 4V_{Cr}'''' = 6Fe'_{Cr} + 6O_O^X + 6H_{metal}$$

Relative to the air-air exposures, dual atmosphere exposure widened the differences between non-preoxidized and preoxidized samples. Fe transport increased in non-preoxidized dual atmosphere exposed sample relative to non-preoxidized air-air exposed sample. In addition, the dual atmosphere seemed to cause more voids to form in the surface oxide layer, probably due to steam being released by the water-forming reaction. The non-preoxidized dual atmosphere sample also showed a much thicker chromia-based layer than the preoxidized sample.

Cr was visible in the outer surface of all the samples placed in the dual atmosphere apparatus, independent of preoxidation level or gas composition. Cr was not significant in the outer layers of the laboratory air exposures. It is possible that Cr transport from the steel substrate is enhanced by the moisture content of the gas. It is more likely that chromia is redepositing onto samples during exposure after volatilizing from the apparatus itself, perhaps condensing onto the samples during cooling. The dual atmosphere apparatus is made from chromia-forming steel and Cr is not significantly visible throughout the coating, only at the outer surface.

ASR

As seen in Figure 10, the ASR values for the non-preoxidized sample increased after about 1,400 hours while ASR values for the preoxidized sample remained steady. Electronic conductivity seems to be slightly improved by preoxidation, perhaps because preoxidation establishes a thinner surface oxide layer of mainly $(Co,Mn)_3O_4$. In addition, as can be seen in Figures 3.1-3.7, the non-preoxidized coating becomes much thicker

with time. A thicker coating implies a greater distance for electrons to travel across and therefore increases ASR, which is directly proportional to coating thickness. Improved conductivity has been observed in other preoxidation experiments with 500 hour time spans [19, 25].

The non-preoxidized samples have a surface oxide layer composed of Co, Mn and Fe (as a result of Fe transport) and are thicker than preoxidized sample coatings. Under certain exposure conditions, a one to one ratio of $MnCo_2O_4$ and Mn_2CoO_4 can be extremely conductive relative to Fe Mn oxides and Fe Co oxides [23]. In the first 200 hours of the ASR test, the preoxidized sample has a higher ASR although we know the surface oxide layer is thinner. Fe presence may also improve conductivity due to the presence of more oxidation states in the spinel. In the last 200 hours of the ASR test, the preoxidized sample has a lower ASR. The 1,650 hour oxidation samples exhibit a weak correlation of thicker surface oxide layers with higher ASR. Due to the complexity and changing nature of the oxidation behavior, it is apparent that ASR is affected by a combination of composition and thickness.

EDS elemental line scans of Si seemed to show islands of Si with some small Si peaks visible in areas but not uniformly over the cross section. The Si islands were visible in both the non-preoxidized sample and the 100 hour preoxidized sample. Si is expected to transport to the steel-air interface after long time exposures and to form an electrically insulative silica (SiO_2) layer on the steel surface. Perhaps Si is beginning to transport at 1,650 hours but has not fully formed an insulative layer. The maximum allowable ASR

value is 100 $m\Omega \bullet cm^2$ with cathode contact paste which may increase ASR observed here since platinum paste was used to avoid cathode interactions [39].

Adhesion

The weaker adhesion of the coating onto preoxidized stainless steel suggests that thicker chromia layers can increase chance of delamination. However, preoxidation seems to affect adhesion as well, most likely due to increased thickness of heterogeneous layers, particularly the chromia-based layer at the interface of the stainless steel and the coating.

The Rockwell Indenter study can only qualitatively assess coating adhesion. Adhesion in SOFC interconnects is most strongly affected by relative coefficients of thermal expansion (CTE) of the adjoining parts, especially with thermal cycling during use. Future work may include a more rigorous quantitative characterization of adhesion, as has been done for other coatings [40]. Another approach to assessment of adhesion includes acoustic emission scratch spectrometry. Future work should include more statistically valid adhesion data through repetition and measurement of delaminated areas, as reported elsewhere [41].

CHAPTER 5

CONCLUSIONS

Metallic CoMn coatings were deposited by magnetron sputtering on stainless steel 441HP samples which were preoxidized in 800°C laboratory air for various times. The samples were then annealed in 800°C air. The oxidation behavior in single and dual atmosphere exposures, and ASR were evaluated. Thermogravimetric analysis, phase development and adhesion were also investigated. The following conclusions were summarized in Figure 4.1 and can be stated as:

- In both laboratory air and dual atmosphere exposures, Fe transported into the metal deposited coatings of samples that were not preoxidized while Fe transport was inhibited in metal deposited coatings of preoxidized samples.
- Thinner surface oxide layers were observed in metal deposited coatings on preoxidized samples relative to metal deposited coatings on non-preoxidized samples.
- Less Fe transported into the oxide deposited coatings relative to the metal deposited coatings on non-preoxidized samples but more than into the metal deposited coatings on preoxidized samples.
- Thermogravimetric analysis showed quantitatively that preoxidized coatings oxidize at a substantially slower rate than non-preoxidized coatings.
- Preoxidized samples were relatively less well adhered than non-preoxidized samples.
- The ASR of the non-preoxidized sample began to increase after 1400 hours while the ASR of the preoxidized sample remain fairly constant.

These conclusions have several implications for SOFC interconnects. Thinner coatings of preoxidized samples maintained a lower ASR and may reduce interfacial stress over time between the cathode and the interconnect. Future work should include more statistically significant adhesion studies and longer ASR studies as well as investigation into compatibility between coatings and other SOFC components like electrode and seal materials. A study to investigate the minimum time and temperature needed to establish an oxide layer that can inhibit Cr transport into the coating and reduce the oxidation rate would be beneficial as well as investigation into the effectiveness of a deposited chromia layer. While SOFCs possess many promising attributes, challenges persist and more research and development are needed.

REFERENCES CITED

[1] Barry, Patrick. “Cool Fuel Cells.” NASA Technology. 2003. http://www.nasa.gov/vision/earth/technologies/18mar_fuelcell.html (March 30, 2011).

[2] Fisher, Craig. “Solid Oxide Fuel Cells.” Advanced Ceramics in the UK. 2001. http://people.bath.ac.uk/cf233/sofc.html (March 30, 2011).

[3] Fuel Cell Handbook Morgantown, WV : U.S. Dept. of Energy, Office of Fossil Energy, National Energy Technology Laboratory, (2004).

[4] S. C. Singhal and K. Kendall, *High Temperature Solid Oxide Fuel Cells: Fundamentals, Design and Applications*, Elsevier, New York (2003).

[5] J. Fergus, *Jom*, **59**, 56 (2007).

[6] J. W. Fergus, *Solid State Ionics*, **171**, 1 (2004).

[7] A. Balland, P. Gannon, M. Deibert, S. Chevalier, G. Caboche and S. Fontana, *Surface & Coatings Technology*, **203**, 3291 (2009).

[8] N. Shaigan, W. Qu, D. G. Ivey and W. X. Chen, *Journal of Power Sources*, **195**, 1529 (2010).

[9] Z. G. Yang, *International Materials Reviews*, **53**, 39 (2008).

[10] W. Z. Zhu and S. C. Deevi, *Materials Science and Engineering a-Structural Materials Properties Microstructure and Processing*, **348**, 227 (2003).

[11] W. J. Quadakkers, J. Piron-Abellan, V. Shemet and L. Singheiser, *Materials at High Temperatures*, **20**, 115 (2003).

[12] Y. Zhao and J. W. Fergus, *ECS Transactions* **16**, 57, (2008).

[13] H. Kurokawa, Y. Oyama, K. Kawamura and T. Maruyama, *Journal of the Electrochemical Society*, **151**, A1264 (2004).

[14] J. Fergus, *Proc. Electrochem. Soc.,* **PV 2005-07,** 1806, (2005).

[15] Z. Yang, G. Xia, S. Simner and J. Stevenson, *Journal of the Electrochemical Society*, **152,** A1896 (2005).

[16] J. W. Fergus, *Materials Science and Engineering a-Structural Materials Properties Microstructure and Processing*, **397**, 271 (2005).

[17] Z. Yang, K. Weil, D. Paxton and J. Stevenson, *Journal of the Electrochemical Society*, **150**, A1188 (2003).

[18] P. Gannon, M. Deibert, P. White, R. Smith, H. Chen, W. Priyantha, J. Lucas and V. Gorokhousky, *International Journal of Hydrogen Energy*, **33**, 3991 (2008).

[19] C. C. Mardare, M. Spiegel, A. Savan and A. Ludwig, *Journal of the Electrochemical Society*, **156**, B1431 (2009).

[20] C. Collins, J. Lucas, T. L. Buchanan, M. Kopczyk, A. Kayani, P. E. Gannon, M. C. Deibert, R. J. Smith, D. S. Choi and V. I. Gorokhovsky, *Surface & Coatings Technology*, **201**, 4467 (2006).

[21] H. Kurokawa, C. P. Jacobson, L. C. DeJonghe and S. J. Visco, *Solid State Ionics*, **178**, 287 (2007).

[22] A. Petric and H. Ling, *Journal of the American Ceramic Society*, **90**, 1515 (2007).

[23] Y. Larring and T. Norby, *Journal of the Electrochemical Society*, **147**, 3251 (2000).

[24] X. Montero, F. Tietz, D. Sebold, H. R. Buchkremer, A. Ringuede, M. Cassir, A. Laresgoiti and I. Villarreal, *Journal of Power Sources*, **184**, 172 (2008).

[25] C. Macauley, P.E. Gannon, M.C. Deibert and P. White*, Int. J. of Hydrogen Energy*, In Press 2010.

[26] E. Alvarez, A. Meier, K. Weil, Z. Yang, *Int. J. Appl. Ceram. Technol.*, **8**, 33 (2011).

[27] H. Ebrahimifar, M. Zandrahimi, *Oxid Met.,* **75**, 125 (2011).

[28] N. Birks, G. Meier, F. Pettit, *High-Temperature Oxidation of Metals,* Cambridge University Press, Cambridge (2006).

[29] W. J. Quadakkers, J. Zurek and M. Hansel, *Jom*, **61**, 44 (2009).

[30] P. Gellings, H. Bouwmeester, *The CRC Handbook of Solid State Electrochemistry*, CRC Press, Enschede (1997).

[31] J. Rufner, P. Gannon, P. White, M. Deibert, S. Teintze, R. Smith and H. Chen, *International Journal of Hydrogen Energy*, **33**, 1392 (2008).

[32] P. Gannon, C. Tripp, A. Knospe, C. Ramana, M. Deibert, R. Smith, V. Gorokhovsky, V. Shutthanandan and D. Gelles, *Surface & Coatings Technology*, **188,** 55 (2004).

[33] W. D. Munz, T. Hurkmans, G. Keiren and T. Trinh, *Journal of Vacuum Science & Technology a-Vacuum Surfaces and Films*, **11**, 2583 (1993).

[34] B. Hua, J. A. Pu, W. Gong, J. F. Zhang, F. S. Lu and L. Jian, *Journal of Power Sources*, **185**, 419 (2008).

[35] J. W. Wu, C. D. Johnson, R. S. Gemmen and X. B. Liu, *Journal of Power Sources*, **189**, 1106 (2009).

[36] Z. G. Yang, G. G. Xia, C. M. Wang, Z. M. Nie, J. Templeton, J. W. Stevenson and P. Singh, *Journal of Power Sources*, **183**, 660 (2008).

[37] Z. Yang, M. Walker, P. Singh, J. Stevenson and T. Norby, *Journal of the Electrochemical Society*, **151,** B669 (2004).

[38] B. Tveten, G. Hultquist, T. Norby, *Oxidation of Metals*, **52,** 221, (1999).

[39] W. Z. Zhu and S. C. Deevi, *Materials Research Bulletin*, **38**, 957 (2003).

[40] X. Sun, W. N. Liu, E. Stephens and M. A. Khaleel, *Journal of Power Sources*, **176**, 167 (2008).

[41] A. Vasinonta and J. L. Beuth, *Engineering Fracture Mechanics*, **68**, 843 (2001).